How Does Hurricane Edouard (2014) Evolve toward Symmetry before Rapid Intensification? A High-Resolution Ensemble Study

GEORGE R. ALVEY III

Department of Atmospheric Science, University of Utah, Salt Lake City, Utah, and
Cooperative Institute for Marine and Atmospheric Studies, University of Miami, and NOAA/AOML/HRD, Miami, Florida

ED ZIPSER

Department of Atmospheric Science, University of Utah, Salt Lake City, Utah

JONATHAN ZAWISLAK

Cooperative Institute for Marine and Atmospheric Studies, University of Miami, and NOAA/AOML/HRD, Miami, Florida

(Manuscript received 28 December 2018, in final form 18 October 2019)

ABSTRACT

A 14-member high-resolution ensemble of Edouard (2014), a moderately sheared tropical storm that underwent rapid intensification (RI), is used to determine causes of vortex alignment and precipitation symmetry prior to RI. Half the members intensify similarly to the NHC's best track, while the other seven ensemble members fail to reproduce intensification. Analyses of initial conditions (vertical wind shear, sea surface temperatures, relative humidity, vortex structure) reveal that lower humidity and weaker, more tilted vortices in nonintensifying members likely increase their susceptibility to boundary layer flushing episodes. As the simulations progress, vortex tilt, inner-core humidity, and azimuthal variations in the structure of precipitation best differentiate the two ensemble subsets. Although all members initially are slowly intensifying asymmetric storms, the RI members are unique in that they have more persistent deep convection downshear, which favors vortex alignment via the stretching term and/or precession. As deep convection transitions to stratiform precipitation and anvil clouds in the upshear quadrants, evaporation and sublimation of condensate advected from the downshear quadrants moisten the middle to upper troposphere. This is hypothesized to promote an increase in precipitation symmetrization, a necessary precursor for RI.

1. Introduction

Forecasting and understanding the processes responsible for tropical cyclone (TC) intensity change, particularly rapid intensification (RI), continues to present a unique problem. TCs can undergo a rapid development while embedded in less favorable environments for intensification [i.e., marginal sea surface temperatures (SST), moisture, and moderate vertical wind shear] (Eastin et al. 2005; Reasor et al. 2009; Kieu et al. 2014). Moderately sheared tropical storms like Edouard (2014) and Matthew (2016) are two examples of storms that experienced RI in an apparently marginal environment. Forecasting intensity in these cases remains challenging, as larger vertical wind shear causes greater uncertainty (Zhang and Tao 2013) due to nonlinear feedbacks between complex vortex structures (e.g., tilted or decoupled vortices), asymmetric precipitation processes, and an evolving surrounding environment (Bhatia and Nolan 2013).

It is well known that vertical shear of the horizontal wind typically forces a wavenumber-1 azimuthal asymmetry in the precipitation distribution in TCs (Frank and Ritchie 1999; Corbosiero and Molinari 2002, 2003; Wingo and Cecil 2010; Hence and Houze 2011; Reasor et al. 2013; DeHart et al. 2014; Alvey et al. 2015). Differential advection from vertical wind shear tends to tilt the vortex in the vertical (Jones 2000) triggering precipitation initiation downshear right (DSR), maxima downshear left (DSL), and minima in the upshear quadrants (Hence and Houze 2011). Because these quadrant asymmetries dominate newly formed, sheared

Corresponding author: George R. Alvey III, george.alvey@noaa.gov

DOI: 10.1175/JAS-D-18-0355.1

storms (Corbosiero and Molinari 2002; Molinari and Vollaro 2010), azimuthally averaged analyses are not as useful for analyzing structural changes.

The detrimental effects of strong vertical wind shear have been well documented (e.g., Demaria and Kaplan 1994; Frank and Ritchie 2001). Simpson and Riehl (1958) first hypothesized that vertical wind shear unfavorably ventilates the TC with dry environmental air at midlevels (Cram et al. 2007; Marín et al. 2009). In addition, evaporative cooling within downdrafts transports this low-entropy air into the boundary layer (Powell 1990; Riemer et al. 2010; Tang and Emanuel 2010, 2012). Some recent studies, however, have offered some competing evidence that TCs can intensify under what was previously considered less favorable environments, that is, moderate 850–200-hPa vertical wind shear of 6–10 $m\,s^{-1}$ (Molinari and Vollaro 2010; Stevenson et al. 2014; Rios-Berrios et al. 2016a,b). Finocchio et al. (2016), Onderlinde and Nolan (2017), and Ryglicki et al. (2018a,b) further demonstrated that because the vertical wind shear may have horizontal and vertical irregularities, large annuli calculations differencing only two vertical levels may not be sufficient.

Sheared TCs often initially have a vertically displaced or tilted vortex that for RI cases becomes aligned near onset (Munsell et al. 2017; Chen et al. 2018; Leighton et al. 2018). A vertically aligned vortex promotes a deeper secondary circulation (Riemer et al. 2010; Rogers et al. 2015); though the process by which a tilted vortex aligns remains unknown. Reasor et al. (2004) demonstrated that the vortex initially tilts downshear, which typically coincides with the precipitation maxima. As the vortex intensifies the tilt vector precesses cyclonically upshear; Schecter and Montgomery (2004) attribute this alignment to damping of vortex Rossby waves. Miyamoto and Nolan (2018), on the other hand, determined in an ensemble of idealized simulations that a vertically upright vortex results primarily from deep convection via a ''bottom-up'' pathway without precession.

While several previous modeling and observational airborne studies have placed more focus on the role of intense, deep convection (Braun et al. 2006; Guimond et al. 2010; Molinari and Vollaro 2010; Molinari et al. 2013; Rogers et al. 2013, 2015, 2016), satellite-based studies emphasize the role of other precipitation modes (i.e., stratiform, shallow, moderately deep convection) for TC intensification. Specifically, an increase in the azimuthal distribution of shallow to moderate precipitation, particularly in the upshear quadrants, has been linked to future intensification (Zagrodnik and Jiang 2014; Tao and Jiang 2015; Alvey et al. 2015; Tao et al. 2017; Fischer et al. 2018). An apparent difference in the relative contributions between deep convection and other precipitation modes, however, probably only reflects the varying characteristics of the observing and modeling system, each having noteworthy deficiencies. Modeling systems tend to have high reflectivity biases (Varble et al. 2014), while observational airborne case studies primarily examine TCs already undergoing intensification (Rogers et al. 2016). Although satellites offer a more robust dataset for storms preintensification, the larger footprint of many sensors may cause undersampling of intense convection (Alvey et al. 2015).

Despite progress in recent years, fundamental questions remain unanswered regarding the relationships between precipitation and intensity change when TCs are experiencing at least moderate vertical wind shear. It is likely that both asymmetric deep convective bursts and symmetrization of other precipitation modes play key roles in the intensification pathway (Guimond et al. 2016). To verify this hypothesis, in this study we attempt to answer the following questions:

1) What are the dominant precipitation types, their spatial distributions, and the evolution of these features with respect to alignment and TC intensification?
2) What causes an azimuthal increase in precipitation, particularly in the upshear quadrants?
3) What is the relationship between vortex alignment and increased azimuthal precipitation symmetry upshear?

This study will complement the observational approach taken in Zawislak et al. (2016) and Rogers et al. (2016) to analyze the processes responsible for Hurricane Edouard's (2014) intensification in moderate vertical wind shear. These previous studies synthesized satellite and airborne observations from multiple aircraft (NASA Global Hawk, NOAA P-3, and NOAA G-IV), during periods before and after intensification, in a shear-relative framework. One of the more significant results was an increase in humidity in the upshear quadrants, prior to and during Edouard's intensification, which was nearly coincident with an increase in precipitation symmetry (Zawislak et al. 2016). However, the precipitation was only inferred to be responsible for the observed humidity increase. Nguyen et al. (2017) further expanded on the Edouard observational results with case studies of other moderately sheared TCs, Bertha (2014) and Cristobal (2014), hypothesizing that reduced midtropospheric humidity causes convective downdrafts with more detrimental boundary layer impacts.

From the observational studies it is clear that an increase in humidity upshear is a key factor in intensification in vertical shear. What is not known, however, are the sources of this humidification. This study will address multiple hypotheses regarding potential sources of upshear, mid- to upper-tropospheric humidity increases:

1) Detrainment from convection or evaporation of stratiform precipitation

2) Decreasing lateral entrainment of unfavorable, dry air from the environment
3) Vortex alignment that promotes more efficient inner-core midtropospheric water vapor advection from downshear to upshear

This study advantageously uses perturbed initial conditions much like Rios-Berrios et al. (2016a,b), Munsell et al. (2017), and Leighton et al. (2018) to produce an ensemble with a spread of intensity outcomes: some that intensify, and others that do not. Although Munsell et al. (2017) and Leighton et al. (2018) demonstrate the importance of vortex alignment and precipitation symmetry, this study builds upon those previous studies by exploring the causes of precipitation symmetrization. The unique usage of water vapor mixing ratio budgets help identify humidification sources upshear, one hypothesized cause of precipitation symmetrization. In addition, we compare the temporal evolution of precipitation symmetrization to the inner-core humidity before, during, and after vortex alignment.

2. Data and methods

a. Edouard (2014) synopsis

Edouard was designated a tropical depression by the National Hurricane Center at 1200 UTC 11 September, and reached tropical storm strength 12 h later (Stewart 2014). Over the next 24–48 h, Edouard slowly intensified [$<7.5\,m\,s^{-1}$ $(24\,h)^{-1}$] under the presence of moderate (8–10 $m\,s^{-1}$) deep-layer vertical wind shear and marginally conducive SSTs (Zawislak et al. 2016). According to the best track, Edouard experienced a period of RI [$13\,m\,s^{-1}$ $(24\,h)^{-1}$], from 1200 UTC 13 September through 14 September.

b. Experimental setup

Initial and lateral boundary conditions from 14 Global Ensemble Forecast System (GEFS) members from the 1200 UTC 11 September model cycle are simulated by the Advanced Research version of the Weather Research and Forecasting (WRF) Model (ARW; Skamarock et al. 2008), version 3.7.1. Seven members were selected that intensified, while a different seven members were selected that did not. The outer domain (27 km) remains fixed across the North Atlantic Ocean, while the inner three domains follow the 850-hPa vortex. The three two-way nests have a horizontal resolution of 9, 3, and 1 km and 55 vertical levels. SSTs are prescribed using NOAA's real-time, global, daily SST analysis (Reynolds 1988) at 1/12° spatial resolution. The following physics schemes are uniformly chosen for all ensemble members: Thompson microphysics scheme (Thompson et al. 2008), Kain–Fritsch (Kain 2004) cumulus parameterization (27-km mesh only), and Yonsei University (YSU) planetary boundary layer scheme (Hong et al. 2006). New variables are added to WRF to directly output water vapor mixing ratio tendencies.

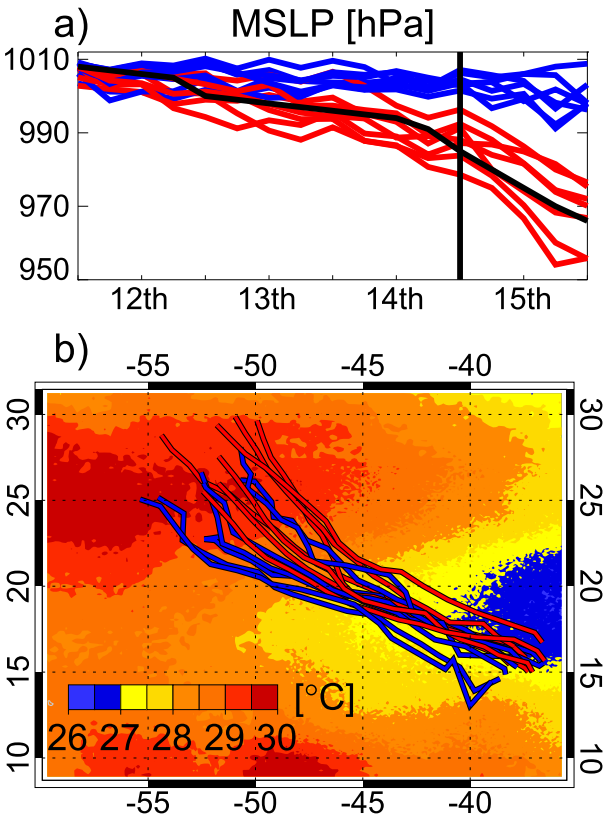

FIG. 1. (a) Minimum sea level pressure (MSLP) for 14 ensemble members with respect to time (x axis; UTC). Blue lines represent failed members and red lines are successful members. The black line is the NHC best track. The black vertical line represents mean RI onset time. (b) Sea surface temperatures (°C) overplotted by the 14 ensemble member tracks.

Ensemble members from the model cycle quickly diverge into a large intensity spread early in Edouard's life cycle as the TC experiences moderate vertical wind shear. Comparisons of members that successfully (S) intensify and those that fail (F) to intensify are used to test the intensification hypotheses described in the introduction. Figure 1a shows the minimum central pressure of the 14 ensemble members with successful members (red lines) experiencing similar intensification as the NHC best track (black line). A cluster of ensemble members that fail to intensify (blue lines) becomes apparent by 0000 UTC 13 September, highlighting the divergence between these two clusters.

c. Analysis techniques

Vortex center locations are calculated at 25 vertical model levels throughout the depth of the troposphere

in 15-min intervals using a variant of Nguyen et al.'s (2014) pressure centroid method. Further details of the methodology can be found in the appendix. While this methodology is not unanimously the best for center identification (Nguyen et al. 2014; Ryglicki and Hart 2015), the dynamic pressure centroid routinely provided the best representation for the weak vortex structures in this ensemble study.

We then calculate the 850–200-hPa vertical wind shear over radii of 0–500-km and rotate variables with respect to the shear direction (i.e., shear-relative coordinates). We generate composite analyses, averaging variables over a relatively large radius within 200 km of the surface center (i.e., inner core) to capture the mid- to upper-level vortex tilt during the early stages of TC development.

Kaplan and DeMaria (2003) classify RI as the 95th percentile of 24-h intensity changes. For continuity with recent studies, we also classify Edouard's intensification period as RI as its 13 m s^{-1} in 24 h (or −23 hPa in 24 h) intensification rate is the 95th percentile of 24-h intensity changes within the ensemble. Rather than analyze TCs with respect to RI onset (Zagrodnik and Jiang 2014; Tao and Jiang 2015; Munsell et al. 2017; Leighton et al. 2018; Miyamoto and Nolan 2018), here, we consider a coherent, relatively aligned vortex a critical characteristic of storms that experience RI. Therefore, analyses focus on the timing relative to the vortex alignment, rather than RI onset.

To our knowledge no study has quantified the timing of alignment despite recognition of its importance (Schecter et al. 2002; Reasor et al. 2004; Reasor and Eastin 2012; Rappin and Nolan 2012; Munsell et al. 2017; Leighton et al. 2018; Miyamoto and Nolan 2018; Rios-Berrios et al. 2018; Ryglicki et al. 2018a,b). Most previous studies have chosen varying depths between 0 and 8 km to describe the tilt distance (Miyamoto and Nolan 2018, 0–8 km; Leighton et al. 2018, 2–8 km; Smith et al. 2017, 1–8 km; Munsell et al. 2017, 850–500 hPa; Schecter 2017, 0–5.7 km; Ryglicki et al. 2018b, 0–6 km; Rios-Berrios et al. 2018, 900—400 hPa). For this study, we define an "alignment" time using the ratio of the maximum tilt magnitude between the surface and all levels ≤8 km to the radius of maximum winds (RMW), calculated for each time step; we require that the ratio of this threshold remains below 0.75[1] for at least 6 consecutive hours:[2]

$$\frac{\max(\text{tilt}|_{0-z\text{km}})}{\text{RMW}} < 0.75, \quad 0 < z \le 8\,\text{km}.$$

Because the mean 0–8-km tilt magnitude is still 24 km at alignment, this time does not represent a perfectly upright vortex. Withholding the first 24–36 h (spinup) of the simulations, this threshold is sufficient for RI in all but one simulation.[3] We compare processes that occur before, during (section 4a), and after (section 4b) the vortex becomes (relatively) aligned.

3. Ensemble overview

a. Environmental conditions

First, we analyze the relative importance of various environmental conditions during Edouard's intensification: vertical wind shear, SST, and environmental relative humidity (RH). Figure 2 illustrates the 0–500-km deep-layer (850–200-hPa) vertical wind shear magnitude. Initially, the deep-layer vertical wind shear is not different between the successful and failed members. Shear values for successful members are not predominantly less than the failed members until 0000–1200 UTC 14 September. After 1200 UTC 14 September, the deep-layer shear for the failed members, while generally higher than the successful subset, has a large spread, with a couple members exhibiting a shear magnitude similar to the successful runs. This suggests that the deep-layer vertical wind shear alone is not responsible for the success or failure of capturing intensification, and reinforces the importance of also examining the shear profile's vertical depth and horizontal distribution (Onderlinde and Nolan 2017; Finocchio et al. 2016; Ryglicki et al. 2018a,b). Though not unique to successful members, we speculate that Edouard's vertical shear profile, concentrated in the upper troposphere (above ~300–400 hPa, Figs. 2b–d), may have helped enable intensification (Finocchio and Majumdar 2017) despite relatively high shear magnitudes (6–12 m s^{-1}). Somewhat surprisingly, aside from diurnal variations, the shear also features a clear upward trend throughout the intensification period as Edouard approaches a tropical upper-tropospheric trough (TUTT) to the west in all ensemble members. Successful members, however, are able to intensify in the presence of increasing vertical wind shear, as they initially

[1] This factor will vary depending upon the center identification method and has not been tested outside this ensemble framework.

[2] Although failed members do not align, the times at which they attempt alignment (i.e., during a temporary reduction in vortex tilt) are used for comparison with successful members. Minimum 1-hourly periods during which the ratio of 0–8-km tilt to RMW is less than 0.75 are subjectively chosen.

[3] The one ensemble member would fall within threshold if the 6-h requirement was varied by a few hours (longer).

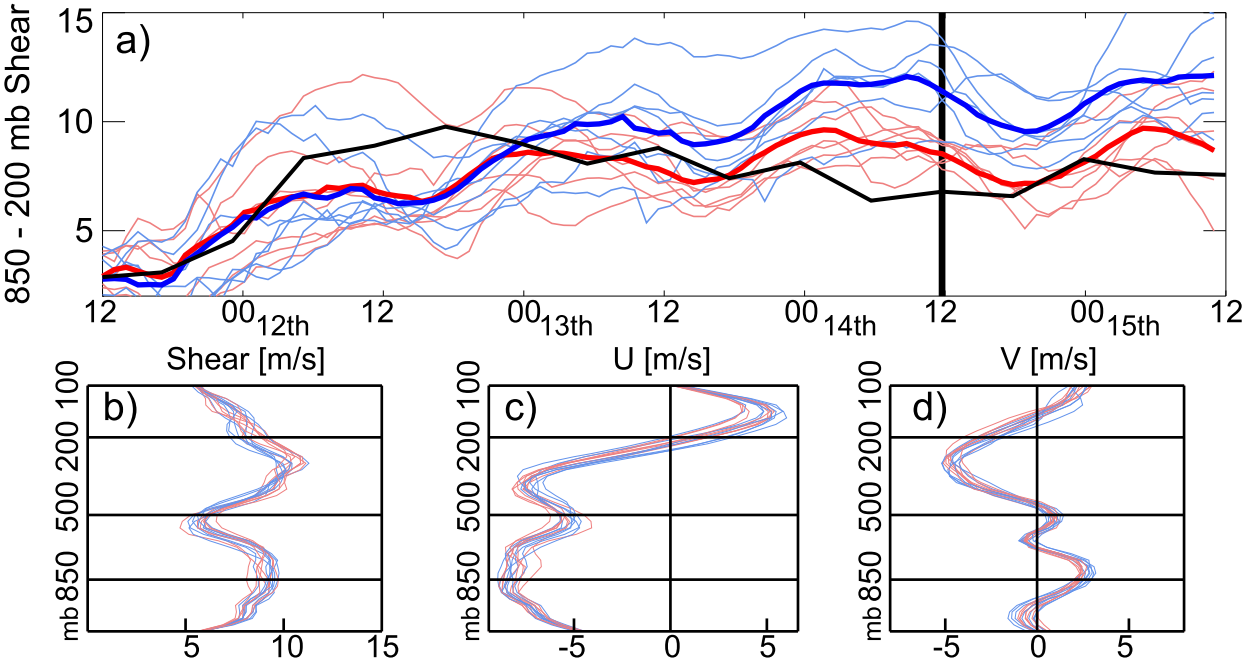

FIG. 2. (a) Deep-layer (850–200 hPa) vertical wind shear ($m\,s^{-1}$), averaged within 0–500 km of the surface center. The red lines depict the successful members and the blue lines depict the failed members, with thick lines representing respective composites. The black line illustrates the Statistical Hurricane Intensity Prediction Scheme's (SHIPS) observed 0–500-km shear (vortex removed, SHDC). The black vertical line represents mean RI onset time. (bottom) Vertical distribution of the (b) shear, (c) zonal wind vector **u**, and (d) meridional wind vector **v** averaged within 0–500 km of the surface center at 0600 UTC 12 Sep.

(11 September–13 September) develop stronger, more resilient vortices (Fig. 3a).

Figure 3b illustrates the 0–500-km azimuthally averaged RH at 1200 UTC 11 September, and shows evidence of being a greater source of initial-condition (IC) differences than seen in the vertical wind shear. While there is still overlap between successful and failed members, successful simulations have significantly greater midlevel (6–8 km) and low-level RH (2–4 km). The GEFS vortex separation technique used in the IC perturbations may contribute to the large member differences in 0–500-km RH and vortex strength. The GEFS version (V10) used in this study utilizes a breeding vector and ensemble transform with the rescaling IC perturbation technique (Tolman 2014), TC relocation, and independent perturbations from the environment (Kurihara et al. 1993; Zhou et al. 2017).

Finally, track differences do not appear to play a large role in the intensity differences between successful and failed members. In fact, the failed members seemingly encounter more favorable SSTs (Figs. 1b, 3c) than the successful members, resulting in initially comparable near-surface equivalent potential temperature θ_E (Fig. 3d) despite weaker surface winds (Fig. 3a). This suggests that ocean temperatures alone do not explain the different outcomes of the ensemble. SSTs remain sufficient for intensification (greater than 26.5°C) throughout the period of interest, and increase on 13–14 September as Edouard traverses SSTs upward of 28°C.

b. *Vortex tilt*

Vortex tilt appears to better differentiate successful and failed members (Fig. 4) than vertical wind shear (Fig. 2), despite some overlap between the two ensemble subsets. The 0–8-km tilt magnitude is noticeably lower for successful members after 0000–1200 UTC 13 September, and precedes any effects from the diverging vertical wind shear magnitudes (Fig. 2) between 0000 and 1200 UTC 14 September. All successful members have an 0–8-km vortex tilt of less than 25 km preceding RI onset. Therefore, according to our ensemble experiment, a relatively aligned vortex with little to no tilt is a necessary condition for RI to occur. This result agrees with other recent studies showing an aligned vortex before or near RI onset (Munsell et al. 2017; Chen et al. 2018; Leighton et al. 2018; Miyamoto and Nolan 2018).

Figure 5 provides a timeline for each successful member that compares the time of vortex alignment and the start of slow intensification (SI) and RI rates. All members begin with an SI period that

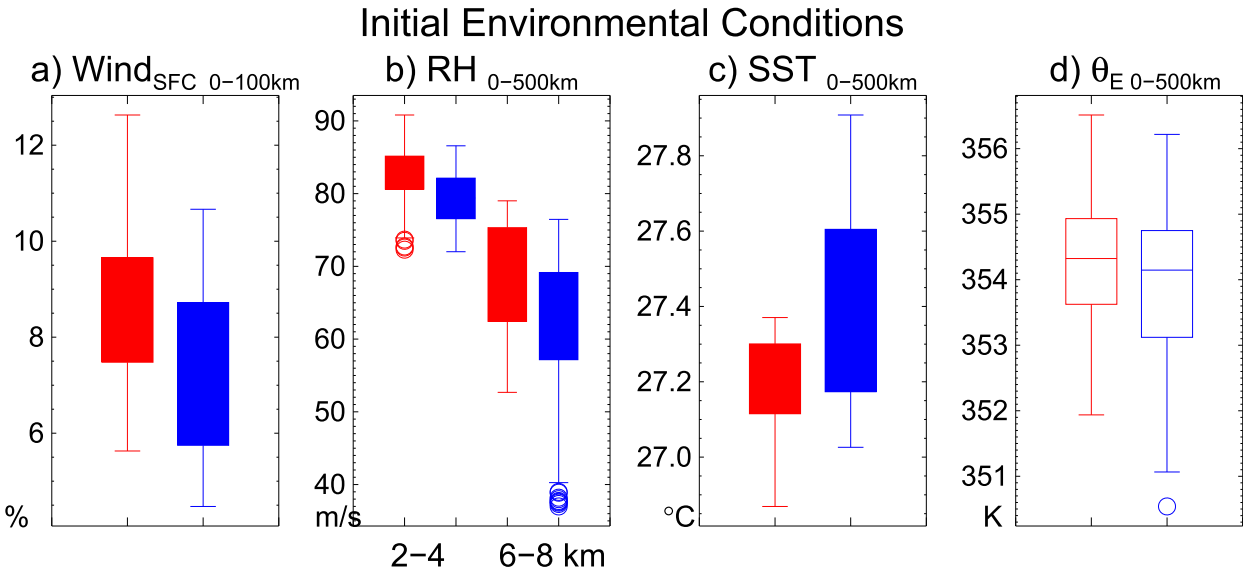

FIG. 3. Box-and-whisker plots of environmental variables, averaged within (a) 100 and (b)–(d) 500 km of the surface center for 1200 UTC 11 Sep–0000 UTC 12 Sep (first 12 h after initialization). Shaded boxes are used when successful members (red) and failed members (blue) are significantly different at the 99% confidence interval (*t* test). The boxes enclose the interquartile range (IQR; 25th–75th percentiles). The whiskers extend to either the maximum (minimum) of data or 1.5 times the upper and lower IQR. Outliers beyond this data are delineated by circles.

precedes the vortex alignment and RI. Most importantly, all successful members that undergo RI (black boxes) achieve an aligned vortex (red boxes) prior to the onset, a result similar to Munsell et al. (2017), Miyamoto and Nolan (2018), and Leighton et al. (2018).

4. Interconnection of vortex alignment, inner-core precipitation, and humidity

a. Prealignment

During the period before alignment, the midlevel center (MLC; 5 km) and upper-level center (ULC; 8 km) typically tilt downshear from the low-level center (LLC; 0–2 km) due to vertical wind shear. This section examines how the successful members evolve from a tilted vortex to one that is vertically upright, with respect to three hypotheses.

1) H1: THE TILTED VORTEX EXHIBITS HORIZONTAL PRECESSION TOWARD THE UPSHEAR QUADRANTS (REASOR ET AL. 2004)

We investigate the vortex structure in more detail in Fig. 6, which shows the shear-relative distribution of the pressure centroids (centers) at all vertical levels. Preceding the 0–8-km alignment by 36 h (Fig. 6a), the 0–8-km tilt exhibits a clockwise curvature with height in which the center progressively tilts radially outward and farther DSR with height. During the following 36 h, ending with alignment, a trend is observed in which the mid and upper-level centers not only become more aligned with the surface center, but also appear to precess cyclonically from the DSR to DSL quadrant. This evolution is not unlike the precession shown in Reasor et al. (2004), Stevenson et al. (2014), and Munsell et al. (2017), only differing in that most members of the successful ensemble do not rotate into the upshear-left (USL) quadrant. In contrast to successful, the failed members not only remain tilted more downshear at larger radial distances with height, but also rarely exhibit a similar rotation toward DSL that the successful members exhibit.

As Figs. 6a–d only shows snapshots, Figs. 6e–g demonstrates more detailed evolution of the 0–8-km tilt vector for a few successful members. At least one simulation (Fig. 6e) aligns without precession, perhaps a result of its initially large tilt and broad vortex structure. Figure 6f, on the other hand, suggests nonmonotonic precession in a different successful member. Other members (i.e., Fig. 6g) not only have an initially large tilt and evolution like Fig. 6e, but also resemble precession after the tilt reduces to $<\sim$50 km. Finally, more erratic tilt evolution with minimal precession is observed in the failed composite (Fig. 6h).

Figures 7a–c shows evidence in another successful member that first the LLC and 5-km MLC move toward

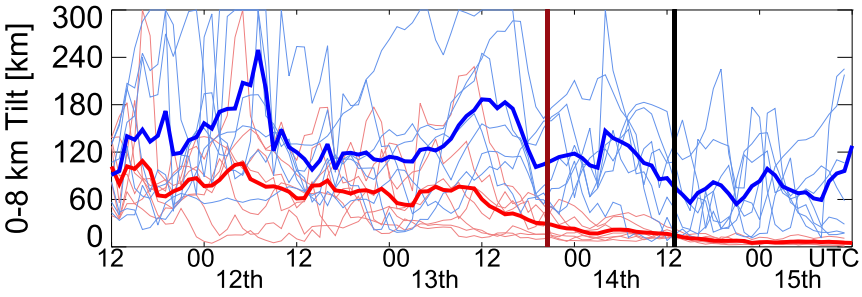

FIG. 4. Vortex tilt between 0 and 8 km for successful member (red thick line) and failed member (blue thick line) composites with thin lines representing individual members. The vertical black (dark red) line represents mean RI onset (alignment) time.

one another without precession. Although the LLC is initially nearly void of precipitation, deep convection increases likely due to enhanced upward motion and surface convergence as the LLC[4] approaches the MLC, an evolution with some similarities to "downshear reformation" observed by Chen et al. (2018) in a RI modeling study. The MLC rotates cyclonically around the LLC only after the 0–5-km tilt reduces to <25–50 km (Figs. 7b,c). A vertical vorticity ζ budget is calculated within 0–50 km of the surface center in a storm-relative SR framework (Montgomery et al. 2006; Fang and Zhang 2011; Raymond et al. 2011; Chen et al. 2018) using Cartesian coordinates with the residual R including solenoidal and diffusion terms:

$$\left.\frac{\partial\zeta}{\partial t}\right|_{\mathrm{SR}} = \underbrace{-u_{\mathrm{SR}}\frac{\partial\zeta}{\partial x} - v_{\mathrm{SR}}\frac{\partial\zeta}{\partial y}}_{\mathrm{Advection}_{xy}} \underbrace{- w\frac{\partial\zeta}{\partial z}}_{\mathrm{Advection}_{z}} \underbrace{- (\zeta + f)\left(\frac{\partial u_{\mathrm{SR}}}{\partial x} + \frac{\partial v_{\mathrm{SR}}}{\partial y}\right)}_{\mathrm{Stretching}} \underbrace{- \left(\frac{\partial v}{\partial z}\frac{\partial w}{\partial x} - \frac{\partial u}{\partial z}\frac{\partial w}{\partial y}\right)}_{\mathrm{Tilting}} + R.$$

Through an analysis of the budget terms, the alignment is preceded by an increase in vorticity magnitude (Fig. 7d) throughout the troposphere. Initially, the vorticity stretching (Fig. 7f) term below 2 km increases from 44 to 56 h as deep convection more persistently develops downshear. Meanwhile, vorticity in the mid- to upper levels increases predominantly due to horizontal advection (Fig. 7e) as the LLC and MLC precess toward one another. As the vortex nears alignment (56 h), precipitation coverage continues to increase (Fig. 7c) coinciding with larger mid–upper-tropospheric vorticity contributions from vertical advection and tilting, followed by stretching.

In contrast, the failed member (Figs. 7g–i) attempts to align, but most of the deep convection that develops near the center is transient. The stretching term does increase at 58 h, but like other failed members it decreases as the deep convection lacks persistence near the LLC and MLC. The mid- to upper-level vorticity also unfavorably decreases after 58 h as negative horizontal advection (Fig. 7k), and the lack of deep convection contributes to a displacement of the MLC DSR due to shear.

In summary, some successful members resemble vortex precession (H1); however, a majority of members do not propagate entirely upshear. And other successful members align primarily by vortex stretching from convection or a combination of both stretching and precession indicating that no singular pathway to alignment exists.

2) H2: SHALLOW AND MODERATELY DEEP PRECIPITATION USL (NGUYEN ET AL. 2017) TRANSITIONS INTO STRONGER, DEEP CONVECTIVE UPDRAFTS INTENSIFYING A VORTEX THROUGH A BOTTOM-UP PATHWAY (MONTGOMERY ET AL. 2006)

The azimuthal location, radial distance from the center, and intensity of precipitation play important roles in TC intensification. Figure 8a shows a Hovmöller of the mean inner-core precipitation [i.e., rain rate (RR)] for all successful members relative to the shear-relative azimuthal distribution. Hereafter, inner core refers to 200-km radial averages with respect to the surface center unless otherwise stated. Commonly seen with sheared tropical storms (Reasor et al. 2000), Edouard features a distinct wavenumber-1 asymmetry with deep convection primarily downshear (mean RR > 10 mm h^{-1})

[4] The appearance of the LLC moving toward the MLC is caused by low-level vorticity maxima embedded in the broad LLC rotating toward DSR.

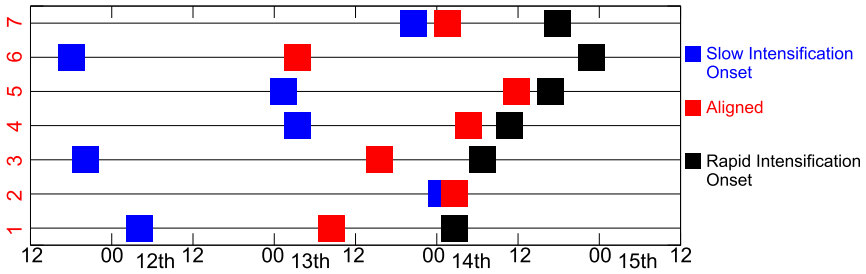

FIG. 5. Timeline for all seven successful members. "Rapid intensification" is defined by the first occurrence of the 95th percentile of 24-h pressure changes within the ensemble or <-23 hPa $(24\,\mathrm{h})^{-1}$. "Slow intensification" is the first occurrence of -11.5 hPa $(24\,\mathrm{h})^{-1}$ for 2 consecutive hours. Following section 2c, "aligned" is defined by the first occurrence of a 0–8-km vortex tilt less than 0.75RMW for 6 consecutive hours.

and a relative minimum USR (mean RR $\leq 2\,\mathrm{mm\,h^{-1}}$). Approximately 12 h before alignment, following an increase in convective intensity, the mean rates in successful members increase from 6–8 to 10–12 $\mathrm{mm\,h^{-1}}$ as precipitation also begins to expand toward the USL quadrant as alignment nears.

In contrast to successful members, the failed precipitation composite with respect to alignment time reveals that deep convection covers a smaller azimuthal range, as it remains confined farther DSR and precipitation does not symmetrize around the center. The mean rain rate shows not only generally lower mean rates in the downshear quadrants (Fig. 8c vs Fig. 8a), but also does not exhibit upshear episodes of convection as seen in successful members.

The convective asymmetry (CA) parameter proposed by Schecter (2013) may also be useful for quantifying symmetrization in inherently asymmetric storms. Using vertically integrated rain mass density σ, $\delta\sigma$ represents CA as a dimensionless ratio of the maximum square root of the azimuthally averaged squared perturbation ($\sigma' = \sigma - \overline{\sigma}$) to the maximum azimuthal average $\overline{\sigma}$, whereby the maximum of numerator ($\max_t$) is taken for all values $0.5 \leq$ radius/RMW ≤ 1.5 and maximum of the denominator ($\max_b$) for $0.5 \leq$ radius/RMW ≤ 4:

$$\delta\sigma = \frac{\max_t\left(\sqrt{\overline{\overline{\sigma'^2}}}\right)}{\max_b(\overline{\sigma})}, \quad \sigma = \int_0^{z_t} q_r \rho \, dz.$$

where z_t is z at the model top, q_r is rainwater mixing ratio, and ρ is density. This metric (Figs. 8e,f) indicates that successful (decrease in asymmetry) and failed (greater asymmetry) composites diverge ~18 h before alignment.

While Fig. 8 illustrates the spatial distribution of precipitation, various types of precipitation structures can contribute to those rain rates. In this study we use a slightly modified methodology from Steiner et al. (1995) to classify precipitation as congestus, deep convection, stratiform, anvil, or nonprecipitating. Any grid cell with simulated radar reflectivity that is >40 dBZ at 2.5 km, or sufficiently greater than nearby pixels [defined as "peakedness" in Steiner et al. (1995)] is classified as convective. Those convective grid cells with a 15-dBZ echo top of <8.5 km are classified as congestus, which is similar to shallow to moderate convection defined by Fritz et al. (2016). Any nonconvective grid cell with 2.5-km reflectivity >10 dBZ is classified as stratiform and any remaining grid cells <10 dBZ at 2.5 km are classified as nonprecipitating. Following Feng et al. (2011), we define the anvil by all nonprecipitating grid cells with any positive reflectivity top >6 km. We are aware that the TC convection is typically sloped downwind in the vertical, which is not accounted for in our classification methodology. While analysis of the algorithm for individual cases produced satisfactory results, it could feasibly cause pixels that are part of sloped convective cells to be classified as stratiform. On the other hand, because this study focuses on the period around tropical storm strength, the weaker winds (advection) and greater eyewall slope, may favor less vertically tilted convection (Rogers 2010; Stern et al. 2014).

Figure 9 shows the percent total areal coverage for inner-core precipitation type classifications within the downshear and upshear quadrants. Before alignment, the composite of successful members indicates a larger areal coverage of convection, stratiform, and anvil downshear than failed members (Figs. 9a,b). Whereas the successful composite's areal coverage of convection increases downshear from ~15% to ~25% (Fig. 9a), the areal coverage of stratiform uniformly remains near 40% (Fig. 9b). The failed composite exhibits downshear convective and stratiform coverages more comparable to the successful composite near alignment time 0 h, but the failed composite precipitation increase tends to be more episodic, lacking persistence.

The upshear quadrants (Figs. 9c,d) in successful members from −36 to −24 h do not have large differences

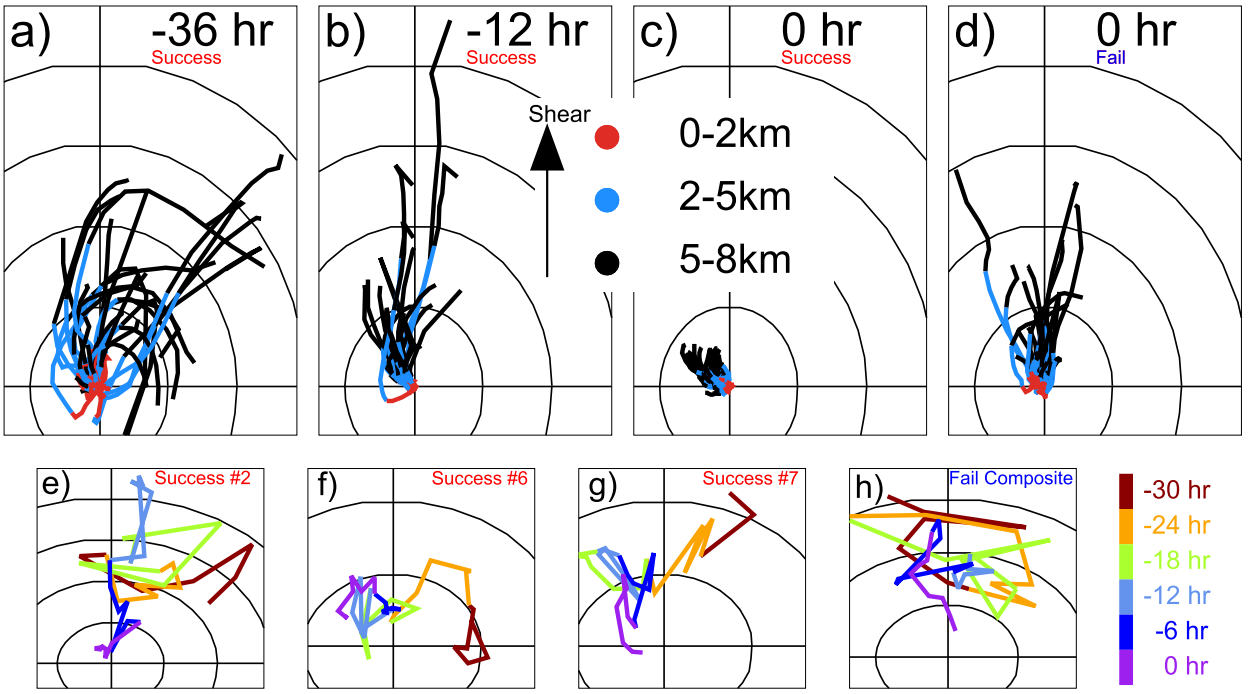

FIG. 6. Vortex tilt with respect to an upward-pointing shear vector for successful members at all 0–8-km vertical levels, within 3 h of (a) −36, (b) −12, and (c) 0 h before alignment. (d) Failed members within 3 h of "alignment" (0 h). Colors represent the 0–2-km (red), 2–5-km (blue), and 5–8-km (black) pressure centroid locations. Intermediate levels are connected by the solid black line in 0.5-km increments. Radii of black circles are in 50-km increments. (e)–(g) Temporal evolution of the 0–8-km tilt vector for three separate successful members color coded by time from −36 to 0 h before alignment. (h) As in (e)–(g), but for the composite of all failed members.

from the failed members. Stratiform and anvil see the strikingly larger increases in fractional occurrence upshear beginning ~18 h before alignment (Fig. 9d). This suggests that as deep convection downshear increases, it begins to rotate upshear and transition into a more stratiform-like precipitation and anvil. Both upshear and downshear congestus make up only a very small portion of the total precipitation (<4% areal coverage). Rather, in contrast to H2, the larger, more apparent prealignment differences between successful and failed composites first appear in the downshear precipitation, followed by differing evolutions (increases) in the anvil and stratiform precipitation upshear.

3) H3: AN MLC-ULC WITH STRATIFORM PRECIPITATION INCREASES LOW–MIDTROPOSPHERIC RH VIA EVAPORATION AND PENETRATES DOWNWARD TOWARD THE BOUNDARY LAYER THROUGH A TOP-DOWN PATHWAY (BISTER AND EMANUEL 1997)

Next, we construct a Hovmöller of inner-core RH (Fig. 10) to relate the evolution of the precipitation with changes in the moisture/humidity for successful members. Consistent with the increase in deep convection (Figs. 8, 9) the RH above 6 km in the DSL quadrant increases (~10%–15%) (Fig. 10a) in the 18-h period prior to alignment. Section 4b will show that this importantly provides a source for subsequent mid- to upper-level horizontal advection of moisture from DSL into the upshear quadrants near and after vertical alignment.

The USL (Fig. 10c) RH, on the other hand, does not increase much above 6 km in the 18 h before alignment. Overall, the USL has lower humidity than DSL above 2 km, which is related to the observed precipitation asymmetry and may at least be partly explained by the upshear, warm anomaly induced by the downshear vortex tilt (Jones 1995). And while high humidity (>70%) consistently extends above 7 km throughout the prealignment period DSL, the USL humidity is consistently ~2–3 km shallower, which is likely reflective of the limited depth of convection in that quadrant. Figure 10e indicates that the largest differences between the successful and failed composite are initially in the upper troposphere (6–12 km) DSL (15%–30% difference), associated with more persistent deep convection than failed members. Composite differences USL (10%–25%) are initially maximized in the midtroposphere (4–8 km) prior to alignment (Fig. 10g), which likely reflects increased shallower precipitation (e.g., stratiform) in those

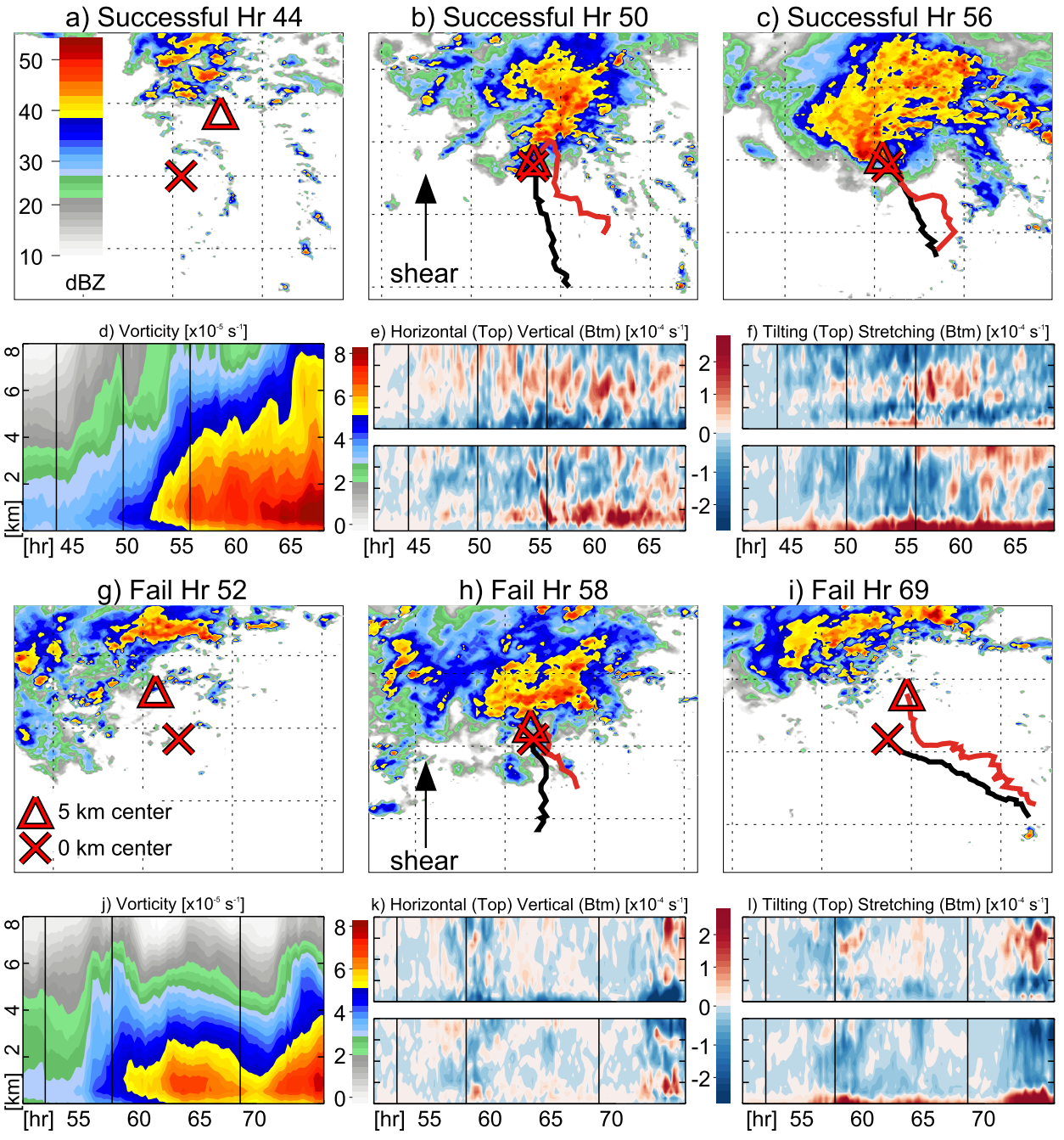

FIG. 7. The 2-km reflectivity for (a)–(c) a successful and (g)–(i) a failed member. The surface center (pressure centroid) is marked by × and the 5-km center with △. In (b), (c), (h), and (i) the tracks from the previous panel time [i.e., h 44–50 for (b)] are shown for the surface center (black line) and 5-km center (red line). Each dotted line in the gridded structure represents 1° of latitude or longitude. (d),(j) Relative vorticity with respect to height averaged within 50 km of the surface center for the successful and failed member, respectively. The vertical black lines coincide with the times of the reflectivity snapshots in (a)–(c) and (g)–(i). (e),(f),(k),(l) Vorticity tendency terms [horizontal advection in (e), top, and (k), top; vertical advection in (e), bottom, and (k), bottom; tilting in (f), top, and (l), top; stretching in (f), bottom, and (l) bottom] with respect to height [as in (d) and (j)] averaged within 50 km of the surface center for the successful and failed member, respectively.

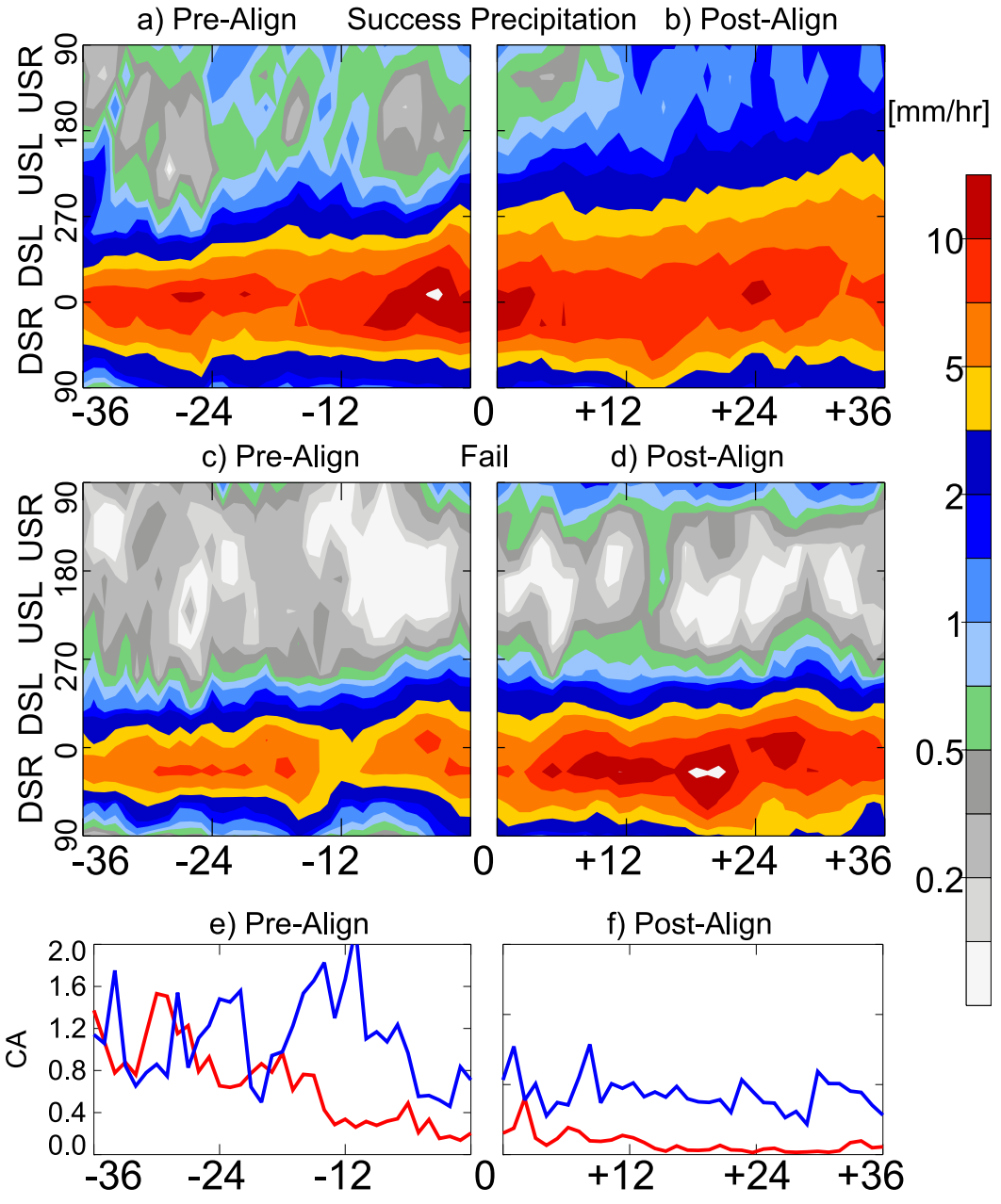

FIG. 8. Composite shear-oriented azimuthal rain-rate Hovmöller diagrams from −36 to +36 h with respect to the alignment time (0 h). Precipitation is averaged within 200 km of the surface center for (a),(b) successful members and (c),(d) failed members. (e),(f) The mean convective asymmetry parameter (CA) is plotted for successful (red) and failed (blue) members.

quadrants in successful members (Fig. 9d). The differences USL also increase above 10 km in the 12 h before alignment, which appears to be related to increases in the areal coverage of anvil in successful members (Fig. 9d). Most importantly, the mid- to upper-tropospheric RH USL increases markedly in successful members (and dries in failed members to a lesser degree) after alignment (Figs. 10c,d), a focus of discussion in section 4b.

The question is, Does an increase in humidity precede changes in the precipitation, or vice versa? To disentangle this relationship, we budget the water vapor mixing ratio microphysics tendencies output from WRF for convection, stratiform, and anvil clouds (Fig. 11). We combine vertical advection and microphysics terms to obtain the effects of convective vertical motion and phase changes on water vapor mixing ratio q_v. In the

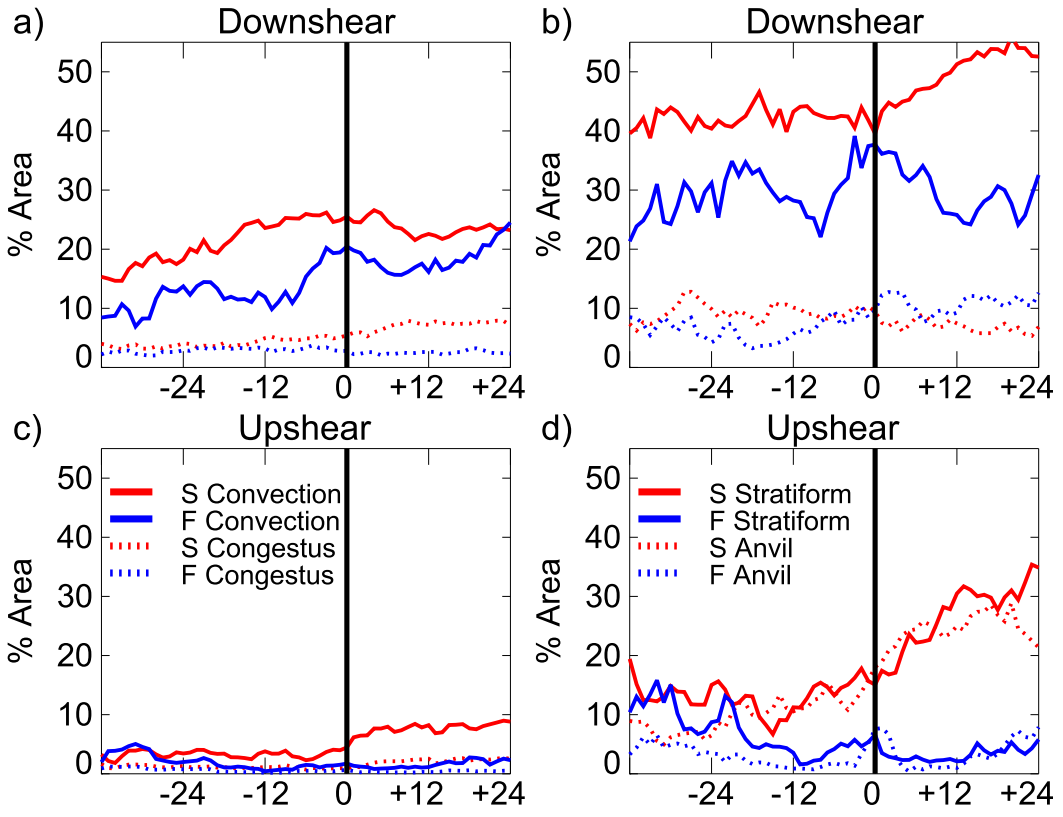

FIG. 9. Fractional areal coverage of precipitation types within 200 km of the surface center, composited for successful (red) and failed (blue) members. Plots are shown with respect to the alignment time, separated into (a),(b) downshear and (c),(d) upshear quadrants. (a),(c) Convection (solid) and congestus (dotted) and (b),(d) stratiform (solid) and anvil (dotted).

period 12 h before alignment, successful simulations have a much greater humidity increase downshear than failed members, primarily resulting from greater areal coverage of convection (Figs. 9a, 11a) and positive horizontal advection of q_v (Fig. 11d). The largest prealignment differences upshear between successful and failed members are greater stratiform precipitation and horizontal advection. While Nguyen et al. (2017) hypothesized that shallow to moderate precipitation is responsible for moistening the USL from the "bottom up," we find that this pathway plays a much smaller role toward increasing humidity and precipitation symmetry. In our results, evaporation from stratiform precipitation provides a significantly greater positive q_v contribution below 5 km. In agreement with H3, these results reflect Bister and Emanuel (1997) and Rappin and Nolan's (2012) "3D showerhead" whereby a decreasing vortex tilt shown in Figs. 4 and 6 promotes condensate advection from downshear to upshear. The humidified environment then favorably allows more sustained convection that propagates farther USL.

Zawislak et al. (2016) and Nguyen et al. (2017) demonstrate that propagation of lower-θ_E air in the form of convective (or mesoscale) downdrafts left of shear can stabilize the boundary layer, suppressing convective development and be a potential hindrance to precipitation symmetry. Figure 12 shows the shear-relative low- to midtropospheric RH (1–4 km) for a composite of four failed members at an average of 21 h (Fig. 12a), 27 h (Fig. 12b), and 37 h (Fig. 12c) after initialization. The time sequence shows that environmental dry low- to midlevel air propagates from the upshear quadrants (>250 km from the center, Fig. 12a) into the right of shear quadrants (150–250 km from the center, Fig. 12b). By 27 h, subsidence increases (1–2 km $w < 0.1\ \mathrm{m\,s^{-1}}$, black contour in Fig. 12b) along the leading edge of the dry-air tongue indicating lateral entrainment into the precipitation (black contour, Fig. 12f). The boundary layer then cools and dries, evidenced by the ~5-K θ_E decrease within 50–250 km of the surface center (Fig. 12g). The resulting stabilization of the boundary layer challenges the ability of surface fluxes to adequately recover the boundary layer to sustain convective development, and likely in conjunction with increasing vertical wind shear

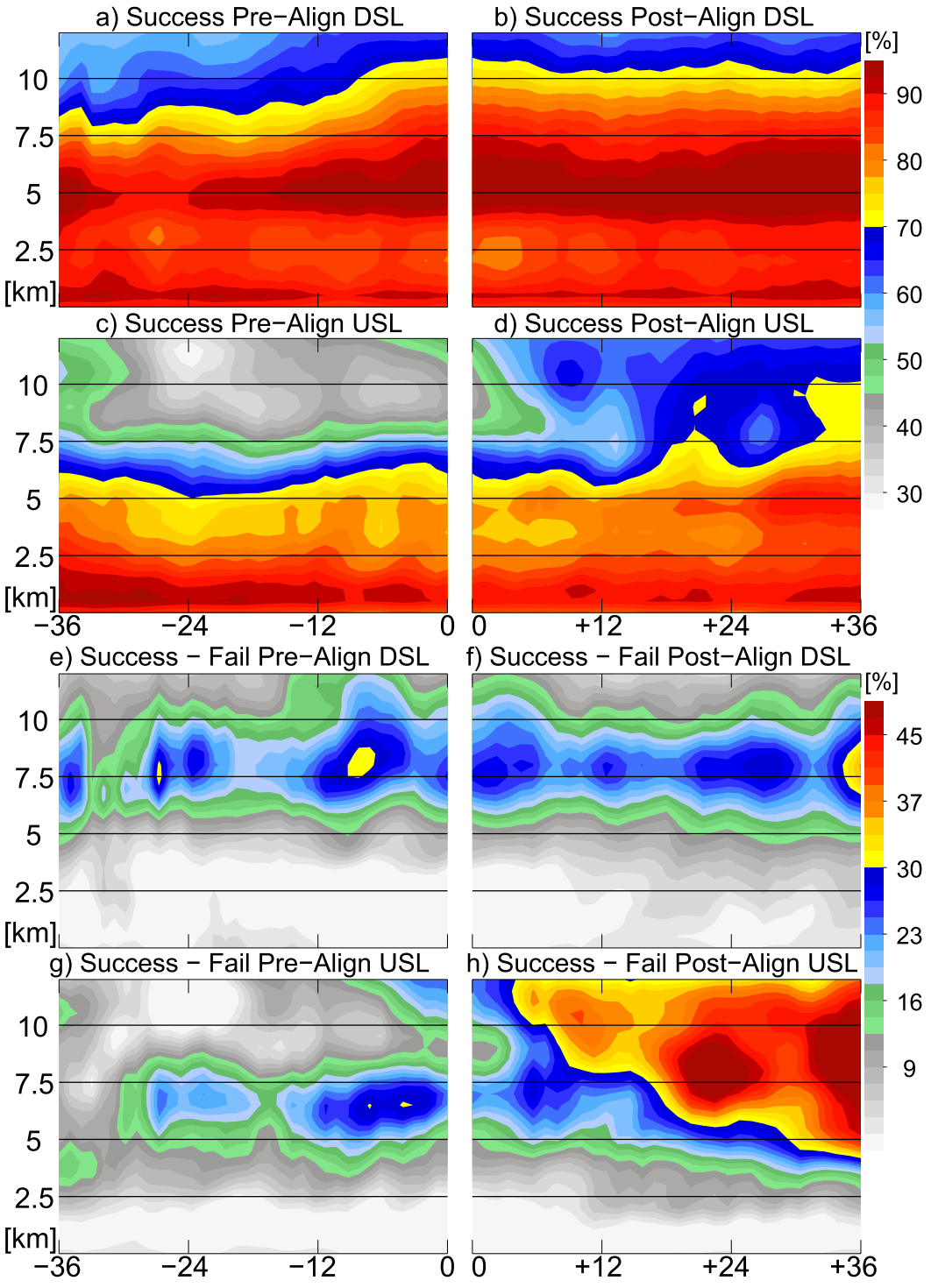

FIG. 10. Composite time series of RH vs altitude for all successful members with respect to alignment (0 h). (a),(b) DSL composite within 200 km of the surface center and (c),(d) USL composite within 200 km of the surface center for (a),(c) prealignment and (b),(d) postalignment periods. (e),(f) DSL successful minus failed member composites and (g),(h) USL success minus failed member composites.

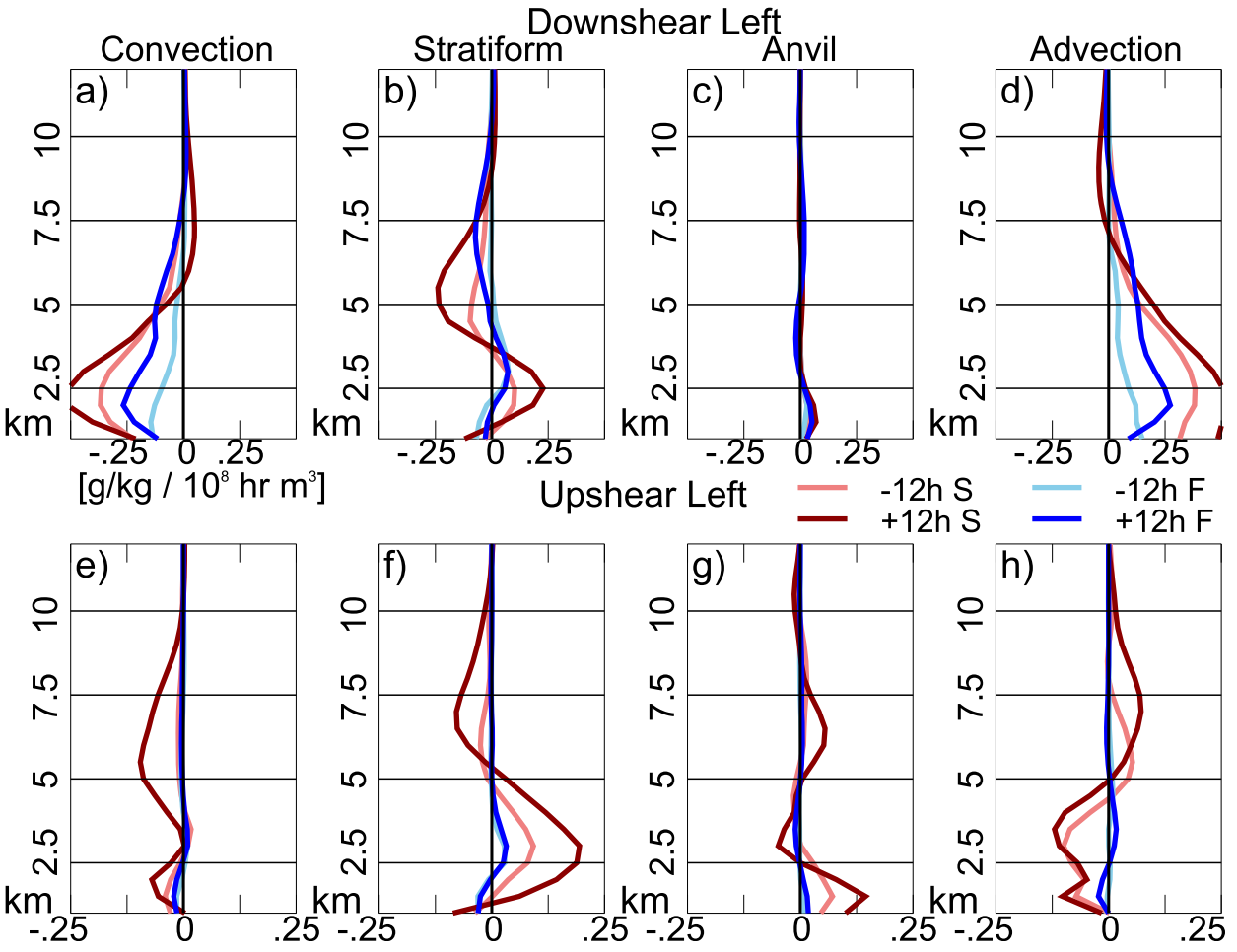

FIG. 11. Combined water vapor mixing ratio contributions from microphysics tendencies and vertical advection. Successful (red) and failed (blue) member composites are divided into (a)–(d) downshear-left and (e)–(h) upshear-left quadrants within 200 km of the surface center. Convection including (a),(e) congestus, (b),(f) stratiform, (c),(g) anvil precipitation types, and (d),(h) horizontal advection are quantified 12 h before alignment (lighter shaded lines) and 12 h postalignment (darker shaded lines).

contributes to the displacement of the precipitation shield (Fig. 12g) 50–100 km farther downshear from the surface center.

Despite also having dry air (Fig. 12d) at larger radii, the successful member composite at 37 h maintains a more humid inner core, possibly owed to the greater inertial stability from stronger initial vortices (Fig. 3a). This may result in a more favorable successful member inner-core thermodynamic environment (greater θ_E) not seen in the failed members until 0000 UTC 14 September, by which point deep-layer shear values (Fig. 2a) have further increased to 8–14 m s^{-1}.

b. *Postalignment*

After Edouard's vortex becomes vertically aligned, precipitation symmetry increases (Fig. 8) and RI commences. While many studies (Alvey et al. 2015; Zawislak et al. 2016; Rogers et al. 2016; Munsell et al. 2017; Miyamoto and Nolan 2018), including this one, have already identified that decreasing vortex tilt and increasing precipitation upshear precedes RI, this study uniquely considers the causes of the precipitation symmetrization. Observations (Zawislak et al. 2016) already suggest a relationship between moistening/humidity increases USL and a precipitation increase USL during this RI period. Here we try to further explain the physical processes behind this relationship.

It is clear from Fig. 8b that the azimuthal symmetry of the precipitation increases substantially, covering nearly all shear-relative quadrants by 24–36 h after alignment. We note, however, that while the precipitation symmetry still increases after the vortex becomes vertically aligned—a result of much greater stratiform precipitation upshear than the prealignment period (Fig. 9d)—the strongest convection (maximum rain rates in Fig. 8b) remains asymmetric. In contrast,

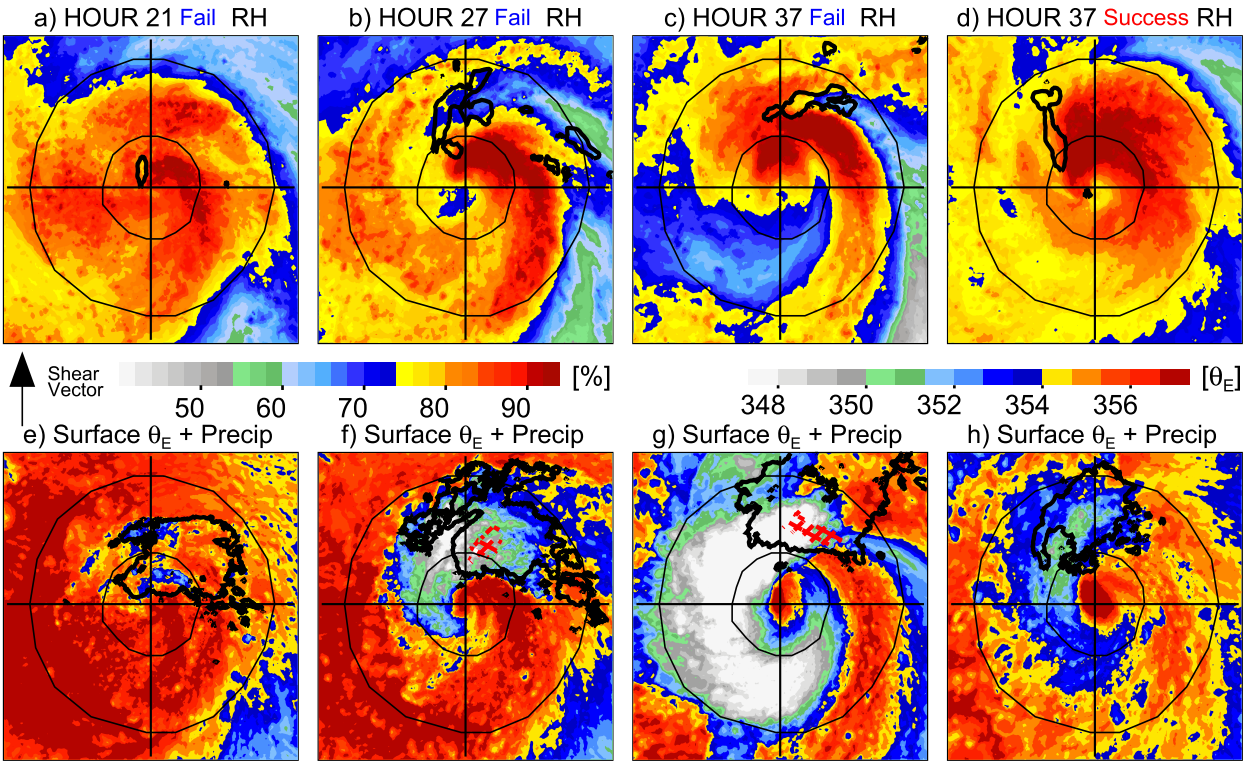

FIG. 12. (top) Shear-relative (shear vector pointing up) 1–4-km layer-averaged relative humidity (color fill) and 1–2-km-layer vertical velocity $<0.1\ \mathrm{m\,s^{-1}}$ (black contour line) for a four-member failed composite at an average of (a) 21, (b) 27, and (c) 37 h after initialization. (d) Successful member composite is 37 h after initialization. Circles are 100- and 250-km radii from the surface center. (bottom) As in the top row, but for shear-relative 2-m θ_E (color fill) and precipitation coverage (black contour line, 3-km dBZ > 20; red hash marks, 3-km dBZ > 40) for a four-member (e) 21-, (f) 27-, and (g) 37-h fail composite, and (h) 37-h successful composite.

because the failed simulations never become vertically aligned (Figs. 4, 6), they fail to sustain precipitation USL and the strongest convection remains confined to DSR.

So how is a vertically aligned vortex more conducive for precipitation symmetry and what role does moisture play? Refer to the postalignment period in Figs. 10b and 10d. In agreement with observational results from Zawislak et al. (2016), mid- (3–6-km) and upper-level (6–12-km) RH increases USL (10%–15% and 20%–25%, respectively) at approximately the onset time of increased precipitation USL (Fig. 8). This RH increase begins prior to RI onset with additional increases in the USL quadrant continuing throughout the RI period. Stratiform precipitation moistens the lower–midtroposphere (Fig. 11f) and anvil clouds (Fig. 11g) moisten the mid- to upper levels (5–8 km). The DSL quadrant RH, in contrast, changes very little after alignment (Fig. 10b). Convection and stratiform provide greater q_v contributions throughout the depth of the troposphere than the prealignment period (Fig. 11); however, the now aligned, stronger vortex also horizontally advects more (and over a greater depth) q_v upshear (Fig. 11h).

Figure 13 illustrates azimuthal precipitation structures and processes that we hypothesize humidify the mid- to upper-tropospheric USL at the alignment time for a successful ensemble member. A reflectivity cross section from DSL to USL (Figs. 13a,b) shows near-center deep convection primarily downshear. A strong, $5\ \mathrm{m\,s^{-1}}$ updraft (Fig. 13e) transports moisture from the lower levels to upper levels (Fig. 13c) where it condenses and/or horizontally advects toward the USL (Fig. 13d). As precipitation rotates toward USL, the vertical velocity (Fig. 13e) profile transitions to one more characteristic of stratiform precipitation. In addition, a positive horizontal q_v advection tendency further aids midtropospheric moistening. Farther USL, the anvil from DSL convection provides additional positive microphysics tendencies from sublimation near the anvil base, an important source for upshear humidification, even without precipitation present.

Previous studies have used similar water vapor tendencies (Fritz and Wang 2014) to examine moistening processes during TC intensification; however, Rios-Berrios et al. (2016b) remains one of the only studies to look at tendencies in a shear-relative framework.

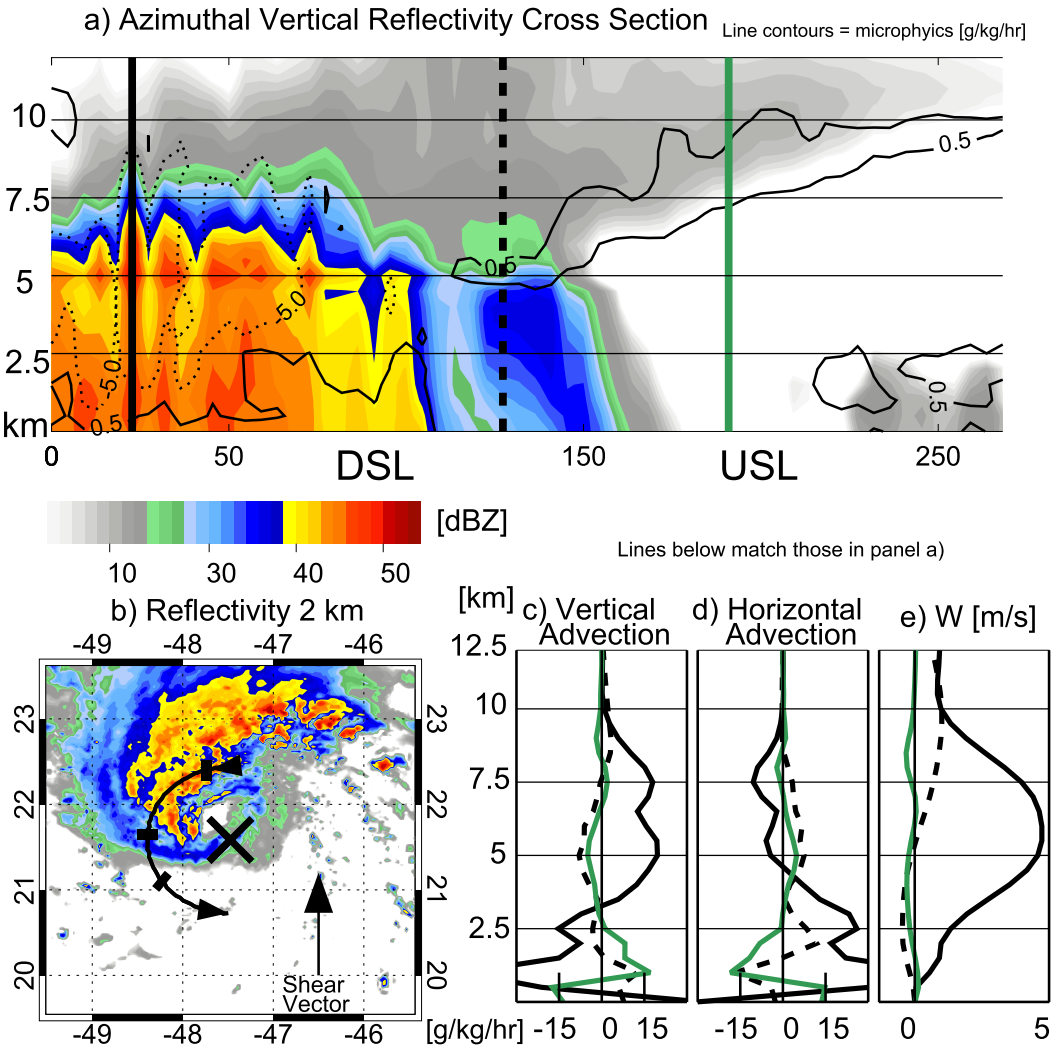

FIG. 13. For successful member 1, for a time period 1 h before alignment, (a) an azimuthal vertical cross section of reflectivity (shading) and q_v microphysics tendencies (g kg^{-1} h^{-1}; line contours) along the curved line from DSL to USL in (b); (b) a plan view of shear-oriented 2.5-km reflectivity ($\times$ denotes the surface center and cross bars correspond to the three vertical transects); and vertical profiles of the (c) vertical advection of q_v, (d) horizontal advection of q_v, and (e) vertical velocity. Line colors in (c)–(e) refer to the vertical transects drawn in various azimuthal locations in (a).

Figure 14 compares the mean composite of inner-core (200-km) q_v tendencies 12 h after alignment for successful members with failed members. The figure shows a result akin to the wavenumber-1 asymmetries seen in the precipitation (Fig. 8) and RH (Fig. 10)—successful member lower–midtropospheric ascent (Fig. 14a, color fill) is primarily confined DSL with subsidence upshear. Strong ascent above 8 km in the upper troposphere indicates the presence of stratiform precipitation USL and "remnant" higher-altitude updrafts from convection originating DSL, a structure similar to one observed in convective bursts (Rogers et al. 2016; Wadler et al. 2018). DSL ascent vertically advects water vapor (Figs. 14a,c; line contours) from the boundary layer to the middle and upper troposphere via convective updrafts (and the secondary circulation). Somewhat surprisingly, failed members have stronger convective updrafts above 5 km (Fig. 14c). Therefore, the most important distinction between those members that intensify from those that do not is the *azimuthal extent* of upper-tropospheric ascent upshear as convection and/or stratiform precipitation propagates farther upshear, not the overall strength of the convection.

Equally important is the horizontal advection of this water vapor from DSL to USL in successful members (Fig. 14b). As condensate horizontally advects USL via stratiform precipitation and anvil clouds (Fig. 11b), it begins to sublimate and evaporate in the relatively dry

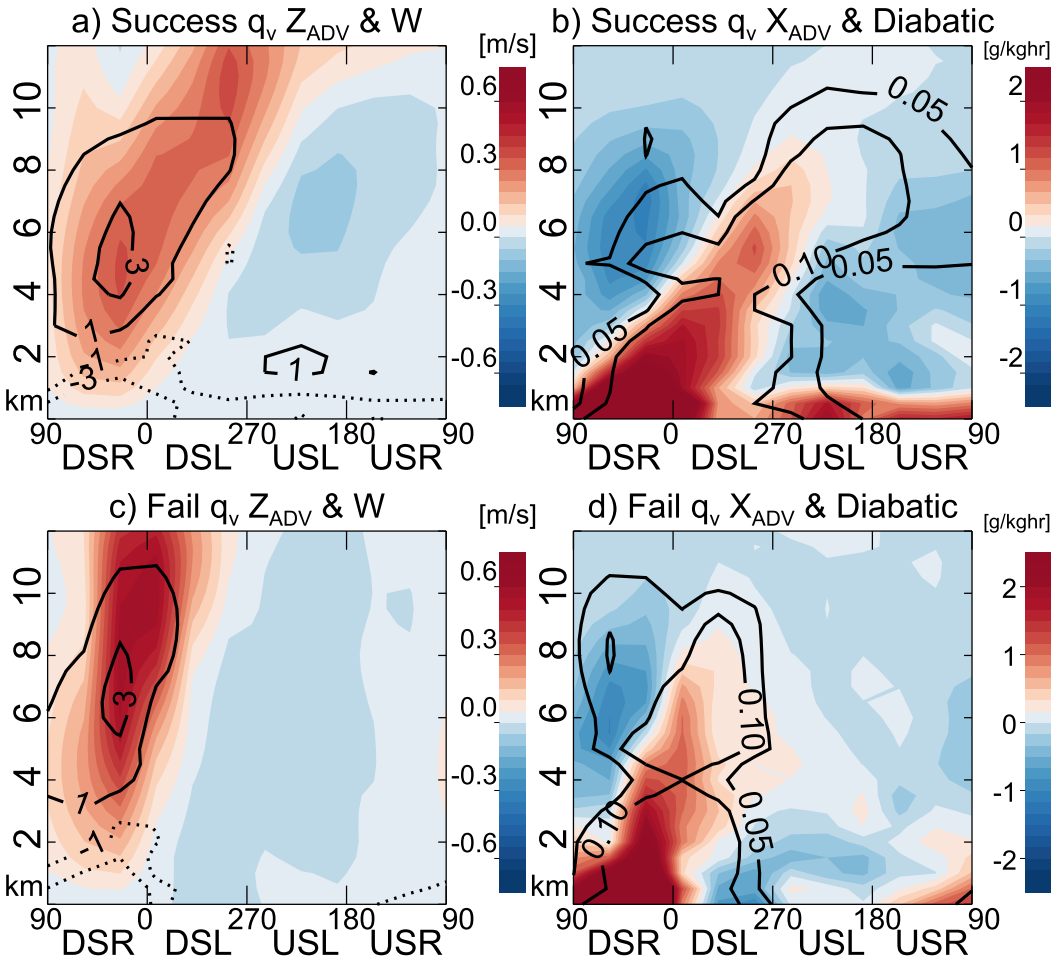

FIG. 14. (a),(b) Successful and (c),(d) failed composite (within 200 km of the surface center) vertical profiles of water vapor (q_v) mixing ratio tendencies 12 h after alignment vs the shear-relative azimuths (quadrants labeled). (a),(c) Mean vertical velocity (W; shaded contours) and q_v vertical advection (Z_{ADV}; line contours). (b),(d) Horizontal q_v advection (X_{ADV}; shaded contours) and q_v rate of change ($g\,kg^{-1}\,h^{-1}$; line contours) from the evaporation and sublimation tendencies (e.g., microphysics parameterization).

upshear quadrants. The q_v contribution eventually forms a feedback loop:

1) The aligned vortex favors precipitation and horizontal water vapor advection DSL to USL in the middle to upper levels.
2) Condensate sublimates and evaporates USL, further moistening the middle to upper troposphere.
3) This more humid environment with less dry air entrainment upshear is hypothesized to favor more persistent precipitation.

Failed members similarly have large positive contributions from midtropospheric horizontal q_v advection but they remain restricted to DSL quadrant. Because condensate cannot advect upshear, significantly less evaporation and sublimation humidifies those quadrants. Given a sufficiently favorable environment in successful members, the above-mentioned cycle continuously feeds back on itself as the vortex intensifies and moisture and precipitation propagate farther upshear with each cycle of convection.

5. Summary

Using a 14-member high-resolution ensemble of Hurricane Edouard (2014), we examined processes responsible for the transition of the storm precipitation from asymmetric to symmetric, while the storm is intensifying within a moderately sheared environment. The 14-member ensemble results in 7 members that closely follow the observed intensification and 7 members that do not reproduce the intensification. Building on other recent ensemble studies (Rios-Berrios et al. 2016a,b; Munsell et al. 2017; Leighton et al. 2018), the

relationships between the large-scale environment, vortex alignment, inner-core thermodynamics, and precipitation processes are investigated by comparing composites of the intensifying and nonintensifying members. In contrast with previous studies, we focus analyses relative to the time of vortex alignment. This study also uniquely uses water vapor mixing ratio budgets in a shear-relative framework in order to test hypotheses linking humidification to increased precipitation symmetry in the upshear quadrants (Zawislak et al. 2016; Nguyen et al. 2017).

The initially greater spread in environmental humidity as compared to the vertical wind shear likely explains a large portion of the ensemble divergence between successful and failed members, a result analogous to Rios-Berrios et al. (2016a,b). Vortex-scale differences also indicate that initially stronger vortices in successful members are more resilient against the increasing wind shear and episodes of lateral dry air entrainment. We speculate that because Edouard's vertical shear profile is concentrated in the upper troposphere (above ~300–400 hPa), outflow near the inner core, potentially from persistent convection DSL, may have more effectively diverted the unfavorable upper-tropospheric environmental winds USL to reduce vertical wind shear[5] and enable intensification in successful members, a hypothesis from a recent study by Ryglicki et al. (2019).

One of the key vortex-scale differences between successful and failed members is that more persistent convection in successful members increases lower-tropospheric vorticity via vortex stretching. As the vortex consolidates and tilt reduces to <50 km, several successful members feature periods of precession between the mid- to upper-level and low-level centers whereas failed members remain tilted downshear right. Differing from previous studies (Rios-Berrios et al. 2016b, 2018; Munsell et al. 2017), most members do not feature a sustained midlevel vortex precession into the USL quadrant[6] and not all successful members exhibit precession prior to alignment. Mechanisms for alignment likely depend on a variety of conditions including the horizontal and vertical vortex structure (i.e., RMW, tilt magnitude, coupledness, size, and depth).

We establish that all ensemble members slowly intensify before the vortex aligns. We also demonstrate that the beginning of precipitation symmetrization coincides with tilt reduction but precedes the time of vortex alignment and increased intensification rates. Symmetry increases more rapidly after alignment, preceding and continuing throughout RI.

We pose a particularly important question regarding the transition toward symmetry: What are the dominant precipitation structures and their azimuthal distributions prior to and during the symmetrization process? Failed members periodically have deep convection increases downshear comparable to successful members, but their convection is displaced farther downshear with the MLC and is less persistent, likely the result of a more stable boundary layer. Updraft dilution and downward fluxes of lower-θ_E air emanate from the entrainment of initially drier low–midtropospheric RH in failed members. This study verifies the importance of precipitation not only DSL, but also its extent USL. With the caveat that this is only one case, the prominent precipitation types USL prior to alignment are stratiform rain[7] and anvil clouds. It is these precipitation structures that result in moistening and RH increases in the upshear quadrants.

Edouard's upshear humidity increase is also seen in an observational study using dropsondes (Zawislak et al. 2016), though spatial and temporally limited observations preclude a determination of the processes responsible for humidification in that study. Results from this study provide evidence that both stratiform precipitation and anvil clouds provide a net moistening, particularly as hydrometeors from DSL deep convection advect USL and fall out in stratiform-like precipitation. In addition, significantly greater increases in horizontal advection of q_v from DSL to USL favor moistening in the middle troposphere, a condition that also favors increasing symmetry and RI. The magnitude of horizontal q_v advection matches the microphysics terms, a result indicating that local storm-scale winds may be equally if not more important. These results are consistent with Bister and Emanuel (1997) and Rappin and Nolan (2012), who hypothesized that stratiform processes and upshear advection of upper-tropospheric frozen condensate moisten the middle troposphere via a "showerhead effect," but differ from pregenesis studies like Fritz and Wang (2014), who emphasized

[5] Because large-annulus vertical-wind-shear calculations currently used may not detect this vertical wind shear reduction (Leighton et al. 2018), we recommend the continued exploration of methodologies like in recent work by Sears and Velden (2012) and Velden and Sears (2014), and emphasize more detailed analysis that better captures the horizontal structure, vertical shape, and local effects from convection.

[6] Centers using potential vorticity centroids also yield a similar lack of propagation upshear.

[7] The stratiform precipitation upshear is likely similar to the "shallow to moderate" precipitation seen in Tao and Jiang (2015), "moderate convection" in Alvey et al. (2015), and "liquid hydrometeors" in Fischer et al. (2018).

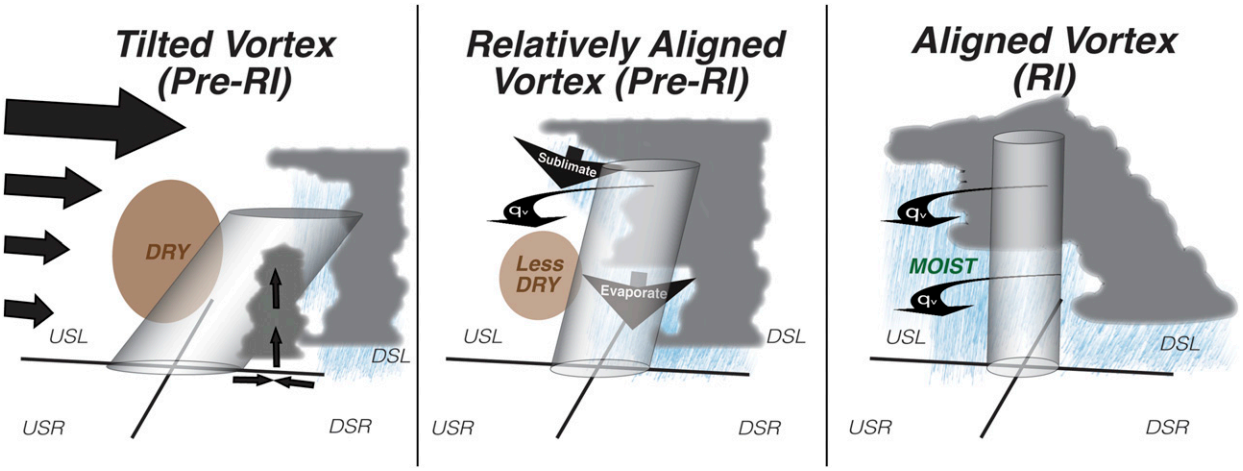

FIG. 15. Schematic demonstrating the shear-relative evolution from (left) a broad, tilted (or decoupled MLC and LLC) vortex to (center) a contracted, upright vortex with mid- to upper-tropospheric moistening USL. (center),(right) Once horizontal advection favors a transition from asymmetric deep convection DSL to stratiform and anvil USL, thermodynamically, this quadrant can better sustain precipitation. The black arrows in the left panel represent the environmental shear.

the role of horizontal moisture influx over nonconvective evaporation.

This ensemble study proposes a pathway for TC intensification in shear, which is summarized with a conceptual model in Fig. 15: An increase in the amount of deep convection DSL occurs in slowly intensifying TCs. A key in sustaining alignment, the persistence of the convection is tied to the background thermodynamic environment (high-θ_E unstable boundary layer and moist midtroposphere). As the vortex aligns (0–8-km tilt reduces to $< \sim$50 km), horizontal water vapor advection from DSL to USL in the mid- to upper levels is favored. Condensate from stratiform precipitation evaporates and anvil clouds sublimates USL, further moistening the middle to upper troposphere. This increased horizontal advection and more humid environment likely favors more sustained convection in the USL quadrants, and more efficient, symmetric latent heating (Nolan et al. 2007; Zagrodnik and Jiang 2014).

Future work will utilize more idealized approaches (i.e., time-varying point downscaling; Onderlinde and Nolan 2017) to test the robustness of results beyond this case study and more directly evaluate the importance of humidification upon precipitation longevity in the upshear quadrants. This study also points to the necessity for operational awareness during these lower-predictability high-shear cases, as suggested by Zhang and Tao (2013). Operational forecasters should diagnose a model spread by not only looking for environmental (i.e., trough or ridge configurations) differences but also the vortex structure (i.e., tilt magnitude, horizontal size, and vertical depth), inner-core midtropospheric humidity, and precipitation evolution by comparing model output to real-time observations. Persistent convection downshear left followed by increases in anvil and stratiform precipitation upshear may provide forecasters an important signal that the vortex is aligning and probability of RI is increasing. Finally, flight patterns for moderately sheared storms should be oriented in a shear-relative framework with a focus on the DSL to USL transition zone and any apparent moisture gradients.

Acknowledgments. This research is supported by NASA HS3 Grants NNX11AB59G, NNG11HG00I, NNX15AN30H, and NASA Research Opportunities in Space and Earth Science (ROSES) Grant 80NSSC19K0012, under the leadership and direction of Dr. Gail Skofronick-Jackson. Discussions with Fuqing Zhang, Adam Varble, and Paul Reasor were helpful during the course of this study. The authors thank Rob Rogers, Frank Marks, and 3 anonymous reviewers whose comments greatly improved the manuscript.

APPENDIX

Centroid Identification Methodology

A "dynamical" azimuthally averaged radius of (storm-relative) maximum winds (RMW) is calculated at a 2-km altitude and used to constrain the circle size with radius R over which the centroid is calculated for each time step. Following Nguyen et al. (2014), the centroid is calculated as follows:

$$\overline{x} = \frac{\sum_{r=0}^{r=R} x_i P_i'}{\sum_{r=0}^{r=R} P_i'} \quad \text{and} \quad \overline{y} = \frac{\sum_{r=0}^{r=R} y_i P_i'}{\sum_{r=0}^{r=R} P_i'}, \quad P_i' = P_{\text{env}} - P_i,$$

where $\overline{x}$ is the longitude, $\overline{y}$ is the latitude, x_i and y_i are the grid points within the circle. Maximum horizontal variations are restricted to 100 km between each 0.5-km vertical model level. Because the identification of the low-level center was erratic at times (in weaker stages), the lowest 3 km utilize a minimum of the boxcar-averaged pressure field where s, the smoothing factor is equal to 25:

$$\frac{1}{s}\sum_{j=0}^{s-1} P_{i+j-s/2},$$

where P is the pressure field. The pressure centroid is still calculated as at all other levels, but the minimum calculated from smoothed fields near the surface is weighted as a monotonically decreasing function with height. Further modifications include a reduction of R by a factor of 0.8 above 8 km and 0.6 above 10 km to help prevent "jumps" in the center identification toward non-TC features (i.e., nearby upper-level low). Comparison with vorticity centroids reveals that this "mass-based" pressure centroid methodology yields smaller tilts. The vorticity centroids tend to be more affected by deep convection displaced farther downshear than the mass-based center.

REFERENCES

Alvey, G. R., III, J. Zawislak, and E. Zipser, 2015: Precipitation properties observed during tropical cyclone intensity change. *Mon. Wea. Rev.*, **143**, 4476–4492, https://doi.org/10.1175/MWR-D-15-0065.1.

Bhatia, K. T., and D. S. Nolan, 2013: Relating the skill of tropical cyclone intensity forecasts to the synoptic environment. *Wea. Forecasting*, **28**, 961–980, https://doi.org/10.1175/WAF-D-12-00110.1.

Bister, M., and K. A. Emanuel, 1997: The genesis of Hurricane Guillermo: TEXMEX analyses and a modeling study. *Mon. Wea. Rev.*, **125**, 2662–2682, https://doi.org/10.1175/1520-0493(1997)125<2662:TGOHGT>2.0.CO;2.

Braun, S. A., M. T. Montgomery, and Z. Pu, 2006: High-resolution simulation of Hurricane Bonnie (1998). Part I: The organization of eyewall vertical motion. *J. Atmos. Sci.*, **63**, 19–42, https://doi.org/10.1175/JAS3598.1.

Chen, X., Y. Wang, J. Fang, and M. Xue, 2018: A numerical study on rapid intensification of Typhoon Vicente (2012) in the South China Sea. Part II: Roles of inner-core processes. *J. Atmos. Sci.*, **75**, 235–255, https://doi.org/10.1175/JAS-D-17-0129.1.

Corbosiero, K. L., and J. Molinari, 2002: The effects of vertical wind shear on the distribution of convection in tropical cyclones. *Mon. Wea. Rev.*, **130**, 2110–2123, https://doi.org/10.1175/1520-0493(2002)130<2110:TEOVWS>2.0.CO;2.

——, and ——, 2003: The relationship between storm motion, vertical wind shear, and convective asymmetries in tropical cyclones. *J. Atmos. Sci.*, **60**, 366–376, https://doi.org/10.1175/1520-0469(2003)060<0366:TRBSMV>2.0.CO;2.

Cram, T. A., J. Persing, M. T. Montgomery, and S. A. Braun, 2007: A Lagrangian trajectory view on transport and mixing processes between the eye, eyewall, and environment using a high-resolution simulation of Hurricane Bonnie (1998). *J. Atmos. Sci.*, **64**, 1835–1856, https://doi.org/10.1175/JAS3921.1.

DeHart, J. C., R. A. Houze Jr., and R. F. Rogers, 2014: Quadrant distribution of tropical cyclone inner-core kinematics in relation to environmental shear. *J. Atmos. Sci.*, **71**, 2713–2732, https://doi.org/10.1175/JAS-D-13-0298.1.

Demaria, M., and J. Kaplan, 1994: Sea surface temperature and the maximum intensity of Atlantic tropical cyclones. *J. Climate*, **7**, 1324–1334, https://doi.org/10.1175/1520-0442(1994)007<1324:SSTATM>2.0.CO;2.

Eastin, M. D., W. M. Gray, and P. G. Black, 2005: Buoyancy of convective vertical motions in the inner core of intense hurricanes. Part II: Case studies. *Mon. Wea. Rev.*, **133**, 209–227, https://doi.org/10.1175/MWR-2849.1.

Fang, J., and F. Zhang, 2011: Evolution of multiscale vortices in the development of Hurricane Dolly (2008). *J. Atmos. Sci.*, **68**, 103–122, https://doi.org/10.1175/2010JAS3522.1.

Feng, Z., X. Dong, B. Xi, C. Schumacher, P. Minnis, and M. Khaiyer, 2011: Top-of-atmosphere radiation budget of convective core/stratiform rain and anvil clouds from deep convective systems. *J. Geophys. Res.*, **116**, D23202, https://doi.org/10.1029/2011JD016451.

Finocchio, P. M., and S. J. Majumdar, 2017: A statistical perspective on wind profiles and vertical wind shear in tropical cyclone environments of the Northern Hemisphere. *Mon. Wea. Rev.*, **145**, 361–378, https://doi.org/10.1175/MWR-D-16-0221.1.

——, ——, D. S. Nolan, and M. Iskandarani, 2016: Idealized tropical cyclone responses to the height and depth of environmental vertical wind shear. *Mon. Wea. Rev.*, **144**, 2155–2175, https://doi.org/10.1175/MWR-D-15-0320.1.

Fischer, M. S., B. H. Tang, K. L. Corbosiero, and C. M. Rozoff, 2018: Normalized convective characteristics of tropical cyclone rapid intensification events in the North Atlantic and eastern North Pacific. *Mon. Wea. Rev.*, **146**, 1133–1155, https://doi.org/10.1175/MWR-D-17-0239.1.

Frank, W. M., and E. A. Ritchie, 1999: Effects of environmental flow upon tropical cyclone structure. *Mon. Wea. Rev.*, **127**, 2044–2061, https://doi.org/10.1175/1520-0493(1999)127<2044:EOEFUT>2.0.CO;2.

——, and ——, 2001: Effects of vertical wind shear on the intensity and structure of numerically simulated hurricanes. *Mon. Wea. Rev.*, **129**, 2249–2269, https://doi.org/10.1175/1520-0493(2001)129<2249:EOVWSO>2.0.CO;2.

Fritz, C., and Z. Wang, 2014: Water vapor budget in a developing tropical cyclone and its implication for tropical cyclone formation. *J. Atmos. Sci.*, **71**, 4321–4332, https://doi.org/10.1175/JAS-D-13-0378.1.

——, ——, S. W. Nesbitt, and T. J. Dunkerton, 2016: Vertical structure and contribution of different types of precipitation during Atlantic tropical cyclone formation as revealed by TRMM PR. *Geophys. Res. Lett.*, **43**, 894–901, https://doi.org/10.1002/2015GL067122.

Guimond, S. R., G. M. Heymsfield, and F. J. Turk, 2010: Multiscale observations of Hurricane Dennis (2005): The effects of hot towers on rapid intensification. *J. Atmos. Sci.*, **67**, 633–654, https://doi.org/10.1175/2009JAS3119.1.

——, ——, P. D. Reasor, and A. C. Didlake, 2016: The rapid intensification of Hurricane Karl (2010): New remote sensing observations of convective bursts from the Global Hawk platform. *J. Atmos. Sci.*, **73**, 3617–3639, https://doi.org/10.1175/JAS-D-16-0026.1.

Hence, D. A., and R. A. Houze Jr., 2011: Vertical structure of hurricane eyewalls as seen by the TRMM Precipitation Radar. *J. Atmos. Sci.*, **68**, 1637–1652, https://doi.org/10.1175/2011JAS3578.1.

Hong, S., Y. Noh, and J. Dudhia, 2006: A new vertical diffusion package with an explicit treatment of entrainment processes. *Mon. Wea. Rev.*, **134**, 2318–2341, https://doi.org/10.1175/MWR3199.1.

Jones, S. C., 1995: The evolution of vortices in vertical shear. I: Initially barotropic vortices. *Quart. J. Roy. Meteor. Soc.*, **121**, 821–851, https://doi.org/10.1002/qj.49712152406.

——, 2000: The evolution of vortices in vertical shear. II: Large-scale asymmetries. *Quart. J. Roy. Meteor. Soc.*, **126**, 3137–3159, https://doi.org/10.1002/qj.49712657008.

Kain, J. S., 2004: The Kain–Fritsch convective parameterization: An update. *J. Appl. Meteor.*, **43**, 170–181, https://doi.org/10.1175/1520-0450(2004)043<0170:TKCPAU>2.0.CO;2.

Kaplan, J., and M. DeMaria, 2003: Large-scale characteristics of rapidly intensifying tropical cyclones in the North Atlantic basin. *Wea. Forecasting*, **18**, 1093–1108, https://doi.org/10.1175/1520-0434(2003)018<1093:LCORIT>2.0.CO;2.

Kieu, C., V. Tallapragada, and W. Hogsett, 2014: Vertical structure of tropical cyclones at onset of the rapid intensification in the HWRF model. *Geophys. Res. Lett.*, **41**, 3298–3306, https://doi.org/10.1002/2014GL059584.

Kurihara, Y., M. A. Bender, and R. J. Ross, 1993: An initialization scheme of hurricane models by vortex specification. *Mon. Wea. Rev.*, **121**, 2030–2045, https://doi.org/10.1175/1520-0493(1993)121<2030:AISOHM>2.0.CO;2.

Leighton, H., S. Gopalakrishnan, J. A. Zhang, R. F. Rogers, Z. Zhang, and V. Tallapragada, 2018: Azimuthal distribution of deep convection, environmental factors, and tropical cyclone rapid intensification: A perspective from HWRF ensemble forecasts of Hurricane Edouard (2014). *J. Atmos. Sci.*, **75**, 275–295, https://doi.org/10.1175/JAS-D-17-0171.1.

Marín, J. C., D. J. Raymond, and G. B. Raga, 2009: Intensification of tropical cyclones in the GFS model. *Atmos. Chem. Phys.*, **9**, 1407–1417, https://doi.org/10.5194/acp-9-1407-2009.

Miyamoto, Y., and D. S. Nolan, 2018: Structural changes preceding rapid intensification in tropical cyclones as shown in a large ensemble of idealized simulations. *J. Atmos. Sci.*, **75**, 555–569, https://doi.org/10.1175/JAS-D-17-0177.1.

Molinari, J., and D. Vollaro, 2010: Rapid intensification of a sheared tropical storm. *Mon. Wea. Rev.*, **138**, 3869–3885, https://doi.org/10.1175/2010MWR3378.1.

——, J. Frank, and D. Vollaro, 2013: Convective bursts, downdraft cooling, and boundary layer recovery in a sheared tropical storm. *Mon. Wea. Rev.*, **141**, 1048–1060, https://doi.org/10.1175/MWR-D-12-00135.1.

Montgomery, M. T., M. E. Nicholls, T. A. Cram, and A. B. Saunders, 2006: A vortical hot tower route to tropical cyclogenesis. *J. Atmos. Sci.*, **63**, 355–386, https://doi.org/10.1175/JAS3604.1.

Munsell, E. B., F. Zhang, J. A. Sippel, S. A. Braun, and Y. Weng, 2017: Dynamics and predictability of the intensification of Hurricane Edouard (2014). *J. Atmos. Sci.*, **74**, 573–595, https://doi.org/10.1175/JAS-D-16-0018.1.

Nguyen, L. T., J. Molinari, and D. Thomas, 2014: Evaluation of tropical cyclone center identification methods in numerical models. *Mon. Wea. Rev.*, **142**, 4326–4339, https://doi.org/10.1175/MWR-D-14-00044.1.

——, R. F. Rogers, and P. D. Reasor, 2017: Thermodynamic and kinematic influences on precipitation symmetry in sheared tropical cyclones: Bertha and Cristobal (2014). *Mon. Wea. Rev.*, **145**, 4423–4446, https://doi.org/10.1175/MWR-D-17-0073.1.

Nolan, D. S., Y. Moon, and D. P. Stern, 2007: Tropical cyclone intensification from asymmetric convection: Energetics and efficiency. *J. Atmos. Sci.*, **64**, 3377–3405, https://doi.org/10.1175/JAS3988.1.

Onderlinde, M. J., and D. S. Nolan, 2017: The tropical cyclone response to changing wind shear using the method of time-varying point-downscaling. *J. Adv. Model. Earth Syst.*, **9**, 908–931, https://doi.org/10.1002/2016MS000796.

Powell, M. D., 1990: Boundary layer structure and dynamics in outer hurricane rainbands. Part II: Downdraft modification and mixed layer recovery. *Mon. Wea. Rev.*, **118**, 918–938, https://doi.org/10.1175/1520-0493(1990)118<0918:BLSADI>2.0.CO;2.

Rappin, E. D., and D. S. Nolan, 2012: The effect of vertical shear orientation on tropical cyclogenesis. *Quart. J. Roy. Meteor. Soc.*, **138**, 1035–1054, https://doi.org/10.1002/qj.977.

Raymond, D. J., S. L. Sessions, and C. López Carrillo, 2011: Thermodynamics of tropical cyclogenesis in the northwest Pacific. *J. Geophys. Res.*, **116**, D18101, https://doi.org/10.1029/2011JD015624.

Reasor, P. D., and M. D. Eastin, 2012: Rapidly intensifying Hurricane Guillermo (1997). Part II: Resilience in shear. *Mon. Wea. Rev.*, **140**, 425–444, https://doi.org/10.1175/MWR-D-11-00080.1.

——, M. T. Montgomery, F. D. Marks, and J. F. Gamache, 2000: Low-wavenumber structure and evolution of the hurricane inner core observed by airborne dual-Doppler radar. *Mon. Wea. Rev.*, **128**, 1653–1680, https://doi.org/10.1175/1520-0493(2000)128<1653:LWSAEO>2.0.CO;2.

——, ——, and L. D. Grasso, 2004: A new look at the problem of tropical cyclones in vertical shear flow: Vortex resiliency. *J. Atmos. Sci.*, **61**, 3–22, https://doi.org/10.1175/1520-0469(2004)061<0003:ANLATP>2.0.CO;2.

——, M. D. Eastin, and J. F. Gamache, 2009: Rapidly intensifying Hurricane Guillermo (1997). Part I: Low-wavenumber structure and evolution. *Mon. Wea. Rev.*, **137**, 603–631, https://doi.org/10.1175/2008MWR2487.1.

——, R. Rogers, and S. Lorsolo, 2013: Environmental flow impacts on tropical cyclone structure diagnosed from airborne Doppler radar composites. *Mon. Wea. Rev.*, **141**, 2949–2969, https://doi.org/10.1175/MWR-D-12-00334.1.

Reynolds, R. W., 1988: A real-time global sea surface temperature analysis. *J. Climate*, **1**, 75–87, https://doi.org/10.1175/1520-0442(1988)001<0075:ARTGSS>2.0.CO;2.

Riemer, M., M. T. Montgomery, and M. E. Nicholls, 2010: A new paradigm for intensity modification of tropical cyclones: Thermodynamic impact of vertical wind shear on the inflow layer. *Atmos. Chem. Phys.*, **10**, 3163–3188, https://doi.org/10.5194/acp-10-3163-2010.

Rios-Berrios, R., R. D. Torn, and C. A. Davis, 2016a: An ensemble approach to investigate tropical cyclone intensification in sheared environments. Part I: Katia (2011). *J. Atmos. Sci.*, **73**, 71–93, https://doi.org/10.1175/JAS-D-15-0052.1.

——, ——, and ——, 2016b: An ensemble approach to investigate tropical cyclone intensification in sheared environments. Part II: Ophelia (2011). *J. Atmos. Sci.*, **73**, 1555–1575, https://doi.org/10.1175/JAS-D-15-0245.1.

——, C. A. Davis, and R. D. Torn, 2018: A hypothesis for the intensification of tropical cyclones under moderate vertical wind shear. *J. Atmos. Sci.*, **75**, 4149–4173, https://doi.org/10.1175/JAS-D-18-0070.1.

Rogers, R., 2010: Convective-scale structure and evolution during a high-resolution simulation of tropical cyclone rapid intensification. *J. Atmos. Sci.*, **67**, 44–70, https://doi.org/10.1175/2009JAS3122.1.

——, P. Reasor, and S. Lorsolo, 2013: Airborne Doppler observations of the inner-core structural differences between intensifying and steady-state tropical cyclones. *Mon. Wea. Rev.*, **141**, 2970–2991, https://doi.org/10.1175/MWR-D-12-00357.1.

——, ——, and J. A. Zhang, 2015: Multiscale structure and evolution of Hurricane Earl (2010) during rapid intensification. *Mon. Wea. Rev.*, **143**, 536–562, https://doi.org/10.1175/MWR-D-14-00175.1.

——, J. A. Zhang, J. Zawislak, H. Jiang, G. R. Alvey, E. J. Zipser, and S. N. Stevenson, 2016: Observations of the structure and evolution of Hurricane Edouard (2014) during intensity change. Part II: Kinematic structure and the distribution of deep convection. *Mon. Wea. Rev.*, **144**, 3355–3376, https://doi.org/10.1175/MWR-D-16-0017.1.

Ryglicki, D. R., and R. E. Hart, 2015: An investigation of center-finding techniques for tropical cyclones in mesoscale models. *J. Appl. Meteor. Climatol.*, **54**, 825–846, https://doi.org/10.1175/JAMC-D-14-0106.1.

——, J. H. Cossuth, D. Hodyss, and J. D. Doyle, 2018a: The unexpected rapid intensification of tropical cyclones in moderate vertical wind shear. Part I: Overview and observations. *Mon. Wea. Rev.*, **146**, 3773–3800, https://doi.org/10.1175/MWR-D-18-0020.1.

——, J. D. Doyle, Y. Jin, D. Hodyss, and J. H. Cossuth, 2018b: The unexpected rapid intensification of tropical cyclones in moderate vertical wind shear. Part II: Vortex tilt. *Mon. Wea. Rev.*, **146**, 3801–3825, https://doi.org/10.1175/MWR-D-18-0021.1.

——, ——, D. Hodyss, J. H. Cossuth, Y. Jin, K. C. Viner, and J. M. Schmidt, 2019: The unexpected rapid intensification of tropical cyclones in moderate vertical wind shear. Part III: Outflow–environment interaction. *Mon. Wea. Rev.*, **147**, 2919–2940, https://doi.org/10.1175/MWR-D-18-0370.1.

Schecter, D. A., 2013: Relationships between convective asymmetry, imbalance and intensity in numerically simulated tropical cyclones. *Tellus*, **65A**, 20168, https://doi.org/10.3402/TELLUSA.V65I0.20168.

——, 2017: A computational study on the nature of meso-ß scale vortex coalescence in a tropical atmosphere. *J. Adv. Model. Earth Syst.*, **9**, 1366–1398, https://doi.org/10.1002/2016MS000777.

——, and M. T. Montgomery, 2004: Damping and pumping of a vortex Rossby wave in a monotonic cyclone: Critical layer stirring versus inertia–buoyancy wave emission. *Phys. Fluids*, **16**, 1334–1348, https://doi.org/10.1063/1.1651485.

——, ——, and P. D. Reasor, 2002: A theory for the vertical alignment of a quasigeostrophic vortex. *J. Atmos. Sci.*, **59**, 150–168, https://doi.org/10.1175/1520-0469(2002)059<0150:ATFTVA>2.0.CO;2.

Sears, J., and C. S. Velden, 2012: Validation of satellite-derived atmospheric motion vectors and analyses around tropical disturbances. *J. Appl. Meteor. Climatol.*, **51**, 1823–1834, https://doi.org/10.1175/JAMC-D-12-024.1.

Simpson, R. H., and H. Riehl, 1958: Mid-tropospheric ventilation as a constraint on Hurricane development and maintenance. *Proc. Tech. Conf. on Hurricanes*, Miami, FL, Amer. Meteor. Soc., D4.1–D4.10.

Skamarock, W. C., and Coauthors, 2008: A description of the Advanced Research WRF version 3. NCAR Tech. Note NCAR/TN-475+STR, 113 pp., http://doi.org/10.5065/D68S4MVH.

Smith, R. K., J. A. Zhang, and M. T. Montgomery, 2017: The dynamics of intensification in a Hurricane Weather Research and Forecasting simulation of Hurricane Earl (2010). *Quart. J. Roy. Meteor. Soc.*, **143**, 293–308, http://doi.org/10.1002/qj.2922.

Steiner, M., R. A. Houze, and S. E. Yuter, 1995: Climatological characterization of three-dimensional storm structure from operational radar and rain gauge data. *J. Appl. Meteor.*, **34**, 1978–2007, https://doi.org/10.1175/1520-0450(1995)034<1978:CCOTDS>2.0.CO;2.

Stern, D. P., J. R. Brisbois, and D. S. Nolan, 2014: An expanded dataset of hurricane eyewall sizes and slopes. *J. Atmos. Sci.*, **71**, 2747–2762, https://doi.org/10.1175/JAS-D-13-0302.1

Stevenson, S. N., K. L. Corbosiero, and J. Molinari, 2014: The convective evolution and rapid intensification of Hurricane Earl (2010). *Mon. Wea. Rev.*, **142**, 4364–4380, https://doi.org/10.1175/MWR-D-14-00078.1.

Stewart, S. R., 2014: National Hurricane Center tropical cyclone report: Hurricane Edouard (AL062014). National Hurricane Center Rep., 19 pp., http://www.nhc.noaa.gov/data/tcr/AL062014_Edouard.pdf.

Tang, B., and K. Emanuel, 2010: Midlevel ventilation's constraint on tropical cyclone intensity. *J. Atmos. Sci.*, **67**, 1817–1830, https://doi.org/10.1175/2010JAS3318.1.

——, and ——, 2012: Sensitivity of tropical cyclone intensity to ventilation in an axisymmetric model. *J. Atmos. Sci.*, **69**, 2394–2413, https://doi.org/10.1175/JAS-D-11-0232.1.

Tao, C., and H. Jiang, 2015: Distributions of shallow to very deep precipitation–convection in rapidly intensifying tropical cyclones. *J. Climate*, **28**, 8791–8824, https://doi.org/10.1175/JCLI-D-14-00448.1.

——, ——, and J. Zawislak, 2017: The relative importance of stratiform and convective rainfall in rapidly intensifying tropical cyclones. *Mon. Wea. Rev.*, **145**, 795–809, https://doi.org/10.1175/MWR-D-16-0316.1.

Thompson, G., P. R. Field, R. M. Rasmussen, and W. D. Hall, 2008: Explicit forecasts of winter precipitation using an improved bulk microphysics scheme. Part II: Implementation of a new snow parameterization. *Mon. Wea. Rev.*, **136**, 5095–5115, https://doi.org/10.1175/2008MWR2387.1.

Tolman, H., 2014: Descriptions of the major modeling systems operated at NOAA/NWS/NCEP. NOAA Rep., 70 pp., https://www.wmo.int/pages/prog/www/DPFS/ProgressReports/2013/documents/2013_USA.pdf.

Varble, A., and Coauthors, 2014: Evaluation of cloud-resolving and limited area model intercomparison simulations using TWP-ICE observations: 1. Deep convective updraft properties. *J. Geophys. Res. Atmos.*, **119**, 13 891–13 918, https://doi.org/10.1002/2013JD021371.

Velden, C. S. and J. Sears, 2014: Computing deep-tropospheric vertical wind shear analyses for tropical cyclone applications: Does the methodology matter? *Wea. Forecasting*, **29**, 1169–1180, https://doi.org/10.1175/WAF-D-13-00147.1.

Wadler, J. B., R. F. Rogers, and P. D. Reasor, 2018: The relationship between spatial variations in the structure of convective bursts and tropical cyclone intensification as determined by airborne Doppler radar. *Mon. Wea. Rev.*, **146**, 761–780, https://doi.org/10.1175/MWR-D-17-0213.1.

Wingo, M. T., and D. J. Cecil, 2010: Effects of vertical wind shear on tropical cyclone precipitation. *Mon. Wea. Rev.*, **138**, 645–662, https://doi.org/10.1175/2009MWR2921.1.

Zagrodnik, J. P., and H. Jiang, 2014: Rainfall, convection, and latent heating distributions in rapidly intensifying tropical cyclones. *J. Atmos. Sci.*, **71**, 2789–2809, https://doi.org/10.1175/JAS-D-13-0314.1.

Zawislak, J., H. Jiang, G. R. Alvey, E. J. Zipser, R. F. Rogers, J. A. Zhang, and S. N. Stevenson, 2016: Observations of the structure and evolution of Hurricane Edouard (2014) during intensity change. Part I: Relationship between the thermodynamic structure and precipitation. *Mon. Wea. Rev.*, **144**, 3333–3354, https://doi.org/10.1175/MWR-D-16-0018.1.

Zhang, F., and D. Tao, 2013: Effects of vertical wind shear on the predictability of tropical cyclones. *J. Atmos. Sci.*, **70**, 975–983, https://doi.org/10.1175/JAS-D-12-0133.1.

Zhou, X., Y. Zhu, D. Hou, Y. Luo, J. Peng, and R. Wobus, 2017: Performance of the new NCEP Global Ensemble Forecast System in a parallel experiment. *Wea. Forecasting*, **32**, 1989–2004, https://doi.org/10.1175/WAF-D-17-0023.1.